RSC Advances

PAPER

View Article Online
View Journal | View Issue

Cite this: *RSC Adv.*, 2025, **15**, 27467

Structural, dielectric, optical, and magnetic properties of ferrite-double perovskites for potential industrial applications

Shubhashree Sahoo,[a] Subhashree Mishra,[a] Harshavardhan Chouhan,[c] Nimai Charana Nayak,[b] Bichitra N. Parida,[c] R. Padhee,[d] S. K. Parida[a] and Rajanikanta Parida *[a]

We report a comprehensive study of the structural, morphological, and electrical properties of the solid-state synthesized perovskite ceramic $Bi_{0.5}Ca_{1.5}Fe_{0.5}Zr_{1.5}O_6$ (BCFZO). A rigorous preparation procedure was carried out, which involved the sintering of the pelletized material, followed by an extensive evaluation utilizing X-ray diffraction (XRD), scanning electron microscopy (SEM), and dielectric studies. The single-phase rhombohedral structure was confirmed by XRD refinement, and SEM demonstrated a clearly defined morphology with an average particle size of 42.068 μm. The investigation of electrical conductivity, which was clarified by Jonscher's universal power law, revealed information about the dynamics of charge carriers that displayed semiconductor behaviour. Intriguing polarization dynamics can be observed by dielectric studies, suggesting potential uses in energy storage. The consistency observed in the charge carrier relaxation process is underscored by the alignment of activation energy values derived from various analyses. The large dielectric constant along with its low loss value and direct optical band gap value of 2.61 eV, present encouraging opportunities for optoelectronic applications. The dielectric complexities of BCFZO open up new possibilities for its application in revolutionary technological fields. The antiferromagnetic behaviour of the transition metal substituted oxide perovskite is governed by the superexchange interactions between two half-filled overlapping atomic orbitals that participate during spin interchange, triggered by the replacement of Zr^{4+} cations at the Fe^{3+} cationic site. The larger value of the thermistor constant as observed in the analysis suggests the potential of this perovskite to be used as an NTC-type thermistor.

Received 25th April 2025
Accepted 18th July 2025

DOI: 10.1039/d5ra02892b

rsc.li/rsc-advances

1. Introduction

Findings from diverse research have revealed promising opportunities for the advancement of new materials featuring superior properties. Scientists have documented that several physical properties can be controlled, including dielectric, magnetic, and electric properties, by precisely adjusting the arrangement and composition of the B and B′ site atoms in oxide-based double perovskite materials.[1–4] Moreover, recent advancements in synthesis techniques allow for greater control over the crystallization process, leading to higher-quality samples with improved structural integrity in the case of different oxide perovskite materials. The interplay between the ferroelectric behavior of A-site cations and the magnetic interactions from B/B′ sites in double perovskite materials hold promise not only for fundamental research but also for practical applications in data storage,[5,6] sensors,[7,8] photovoltaic devices[9] and spintronic devices.[10,11] As we delve deeper into this fascinating area of study, it becomes increasingly clear that understanding these complex interactions will be key to unlocking new functionalities in multiferroic materials. $BiFeO_3$ (BFO) is the most extensively studied of the multiferroic materials, owing to its remarkably high ferroelectric transition temperature (T_c = 1103 K) and ferromagnetic transition temperature (T_N = 643 K).[12] However, the volatility of Bi^{3+} cation is one of the major difficulties in maintaining different properties of the prepared Bi-based perovskites, such as reducing leakage current.

Among all the alternative techniques deployed to reduce the leakage current in the Bismuth ferrite multifunctional material, aliovalent-ion doping is the most fundamental and feasible method rather than thin film formation or rapid liquid phase sintering.[13] Zr doping in $BiFeO_3$ as experimented by S. Mukharjee *et al.* explored the creation of lattice distortion, ultimately

[a]Faculty of Engineering and Technology, Department of Physics, Siksha 'O' Anusandhan (Deemed to be University), Bhubaneswar-751030, India. E-mail: rajanikantaparida@soa.ac.in

[b]Faculty of Engineering and Technology, Department of Chemistry, Siksha 'O' Anusandhan (Deemed to be University), Bhubaneswar-751030, India

[c]Department of Physics, Central Institute of Technology, (Deemed to Be University, Under MoE, Govt. of India), BTR, Kokrajhar, Assam-783370, India

[d]School of Physics, Sambalpur University, Jyoti Vihar Burla-768019, India. E-mail: bichitra72@gmail.com

resulting in a decline in ferroelectric polarisation and a spike in the coercive field.[14] The dielectric data analysis reveals that the doped compositions fail to demonstrate low-frequency relaxation, commonly correlated with defects and grain boundaries. This is evident from the research on the dual cation doping of Pr and Zr in $BiFeO_3$ that the doping attributed to the enhancement of the dielectric properties of the base material due to the demolition of oxygen vacancies during the charge neutralization process of the B-site ion *i.e.*, Zr^{4+} cation.[15] Two different conduction mechanisms were observed inside the grains when the Zr^{4+} ion occupies the Fe^{3+} site based on temperature-dependent DC conductivity determined by impedance and modulus measurement.[16] The anomalous dielectric constant around the Néel temperature implicitly verified the relationship between the magnetic and electric features of $BiFe_{1-x}Zr_xO_3$. Zr^{4+} doped $BiFeO_3$ had a Néel temperature around 20 °C lower than undoped $BiFeO_3$ as experimented by Junjie Xie *et al.*[13] In addition to these outcomes, the primary result of S. M. Abdul Kader *et al.* for the Ba–Zr co-doped single perovskite phase exhibited a spike in electric polarization and magnetization, where the remnant magnetization was approximately 21.8 memu g^{-1}.[17] The general crystal structure *i.e.*, the rhombohedral crystal structure is preserved in this dual cation doped single perovskite without crystal defects showing an equivalence with the reported results for Y–Zr and Ba–Ti doped aliovalent perovskite samples.[17] Due to the notable dielectric characteristics of Ba_2TiZrO_6 double perovskite oxides, Zr doping at the B-site may enhance the dielectric properties of the desired product.[18] A very promising, stable, and functional cathode for solid oxide fuel cells which function at low temperatures (≤500 °C) is Zr and Y co-doped perovskite. Excellent ORR activity, low activation energy, and thermal cycle stability of $BaCo_{0.4}Fe_{0.4}Zr_{0.1}Y_{0.1}O_{3-\delta}$ suggest that this perovskite could be a new cathode potential candidate for commercial Solid Oxide Fuel Cells (SOFC).[19] The $BFe_{0.9}Zr_{0.1}O_{3-\delta}$ (BFZ) synthesized through solid state reaction route by Wei He *et al.* promises to be an intriguing possibility for a symmetrical SOFC electrode due to its strong electrochemical properties and good stability.[20] $BaZr_{0.2}Ti_{0.8}O_3$ (BZT) + $x$$Ba_{0.7}Ca_{0.3}TiO_3$ (BCT) solid solutions were utilised to successfully produce a range of lead-free BaCaZrTi perovskite (BCZT-x) piezoceramics *via* solid-state reaction for the generation of H_2O_2.[21] These investigations suggest that the co-doping of Ca & Zr in $BiFeO_3$-based double perovskite may result in enhanced electrical properties and significant industrial applications.

Perovskite-based materials exemplify great promise for next-generation optoelectronic applications, especially in light-emitting devices, which are anticipated to propel future innovations in the field and their varied applications in sensors, memory devices, energy conversion, and biomedical fields. Reports suggest that by minimising the oxygen vacancies, treating the Bi-site of the antiferromagnetic $BiFeO_3$ with non-magnetic ions such as Pb, Ca, and Sr can boost its ferroelectric behaviour, which opens up the route for the substituted perovskite to be used in device-level implementations.[22]

Double perovskites for visible light photocatalysis promise to have an optimistic outlook. Multiple research efforts have demonstrated the broad spectrum of prospective advantages for double perovskites in solar energy conversion, such as CO_2 reduction, water splitting, and photocatalytic pollution degradation. $BiFe_{0.98}(Zn_{1/2}Zr_{1/2})_{0.02}O_3$, as-synthesised by M. Boukhari, is an appealing selection for photocatalytic and solar cell applications due to its narrow bandgap mediated by the introduction of defect levels that can be a motivation behind the substitution of tetravalent cations.[23]

Despite extensive research on the multiferroic characteristics of doped BFO, experimenting with novel combinations of co-dopants in controlled circumstances can be advantageous. To achieve a beneficial outlook in the modulation of the multiferroic attributes of the earlier described Bismuth ferrite based double ordered perovskite oxides, an alkaline earth metal (Ca) and a transition metal (Zr) are fractionally placed at the A-site and B-site, respectively. The fundamental driving force behind this modification of the parent material into a new ceramic with perovskite arrangements is to attain better properties of double-ordered oxide perovskites with the two-cation substitution at two different cationic sites present in the crystal phase *i.e.*, 12-fold and 6-fold coordinated sites. Their electrical characteristics, such as the dielectric potential, as well as their basic microstructural components, have been extensively studied. Information describing the conduction processes and impedance spectroscopy of the prepared specimen has been included with the Fourier transform infrared spectroscopy (FTIR) spectroscopic study results. A thorough analysis of UV-vis spectroscopy is conducted to assess the compound's sensitivity to em-radiation in the UV-visible spectrum, facilitating its application in optoelectronic devices.

2. Synthesis and characterizations

2.1. Synthesis mechanism

In addition to the excerption process, the manufacturing process of the specimen has considerable effects on its physical characteristics. Finding appropriate raw precursors and a precisely balanced chemical equation are vital processes in synthesizing the converted perovskite material. The basic ingredients used to create the $Bi_{0.5}Ca_{1.5}Fe_{0.5}Zr_{1.5}O_6$ (BCFZO) ceramic were Zirconium dioxide (ZrO_2) (99.50%), ferric oxide (Fe_2O_3) (98.50%), bismuth oxide (Bi_2O_3) (99.50%), and Calcium carbonate ($CaCO_3$) (99.50%) from 'M/S Loba Chemicals Co.' Stoichiometric chemical expression used to produce the desired fractionally substituted oxide double perovskite BCFZO is given below.

$$1.5CaCO_3 + 0.25Fe_2O_3 + 0.25Bi_2O_3 + 1.5ZrO_2 \rightarrow Bi_{0.5}Ca_{1.5}Fe_{0.5}Zr_{1.5}O_6 + 1.5CO_2\uparrow \quad (1)$$

Using the balanced chemical equation, the stoichiometric coefficients, which indicate the mole ratios of reactants and products, are determined. With the mole ratios, the number of moles of the desired product that can be produced from the available moles of reactants is calculated. Extensive computations determined the proper amounts of raw materials required. A chemical weighing scale was used to weigh the parent components as per the established stoichiometry. An agate crusher and pestle had been utilized to crush and blend the precursors for about four hours. The volatile solvent methanol

was subsequently employed to keep the raw components moistened and pestled for a further four to five hours. In a program-monitored furnace, the pestled powder was calcined for 12 hours in a stepwise manner to promote the proper growth of the desired ceramic at 1100 °C. The calcination was done in 4 steps with different dwell times for different temperatures. For the first three temperature increment steps, the dwell time was 1 hour and the temperature was raised from room temperature to 300 °C in 2 hours. Subsequently, in the next steps, temperatures *i.e.*, 500 °C and 800 °C, were achieved in 2 hours for each step and dwell time at those temperatures were also 1 hour. Finally, the last temperature *i.e.*, 1100 °C is incremented in about 2 hour starting from 800 °C and at this temperature the dwell time was 4 hour. This solid-state manufacturing method accommodates the phase growth along with the crystallinity. The phase development of the calcined chemical pestle was confirmed using an X-ray diffractometer at a temperature of 300 K. This analysis produced an X-ray diffraction (XRD) pattern at a scanning speed of 2 deg per min over a range from 20° to 80°. These pellets being pelletized from the calcined ceramic powder were then sintered for a further 12 hours at 1150 °C to amalgamate the pelletized material and eliminate any cover components and non-native particles.

2.2. Characterizations

The crystal structure was analyzed using X-ray diffraction (XRD) of the modified double perovskite, utilizing Cu Kα radiation (λ = 1.5406 Å). The range of Bragg's angles extends from 20° to 80° utilizing a step size of 0.02° per second and a scanning speed of 2° per minute using a 'Rigaku Ultima-IV X-ray diffractometer. Field Emission Scanning Electron Microscopy (FESEM) was employed to carry out the analysis of micro-morphology with the 'Jeol FESEM Model JSM7610F Plus', which operated at an accelerating voltage of 15 kV. Electron Dispersive Spectroscopy (EDS) analysis confirmed the existence of the elemental composition. The FTIR spectra were generated using the Fourier transform infrared spectrometer, specifically the JASCO-FTIR/4100 model. Additionally, the UV-visible diffuse reflection spectroscopy (DRS) spectra of the material were analyzed with the Shimadzu UV-2600i model, covering a wavelength range of 200 to 800 nm. The electrical characteristics of the ceramic pellets, which were coated and silver-pasted, were evaluated at different temperature levels using a highly accurate programmable automatic LCR meter (HIOKI, Model: 1735, Japan) operating across a frequency spectrum of 100 Hz to 5 MHz. The SQUID-VSM DC Magnetometer was used to conduct M–H loop magnetic research at room temperature. Furthermore, Keithley's electrometer (6517B) was used to record *I*–*V* characteristics.

3. Result and discussion

3.1. Structural analysis of BCFZO

3.1.1 X-ray diffraction analysis. By expanding on the foundational insights provided by X-ray diffraction data, we can explore optimization strategies for synthesis methods to improve the crystallinity and overall performance of this promising compound. The fascinating idea of X-ray elastic dispersion is highly beneficial in gathering essential information concerning the intricate aspects of crystallographic structure, including strain, unit cell parameters, crystal defects, and the chemical architecture of the material. Fig. 1(a) depicts the intensity profile obtained from the X-ray diffraction analysis of the sintered pellet

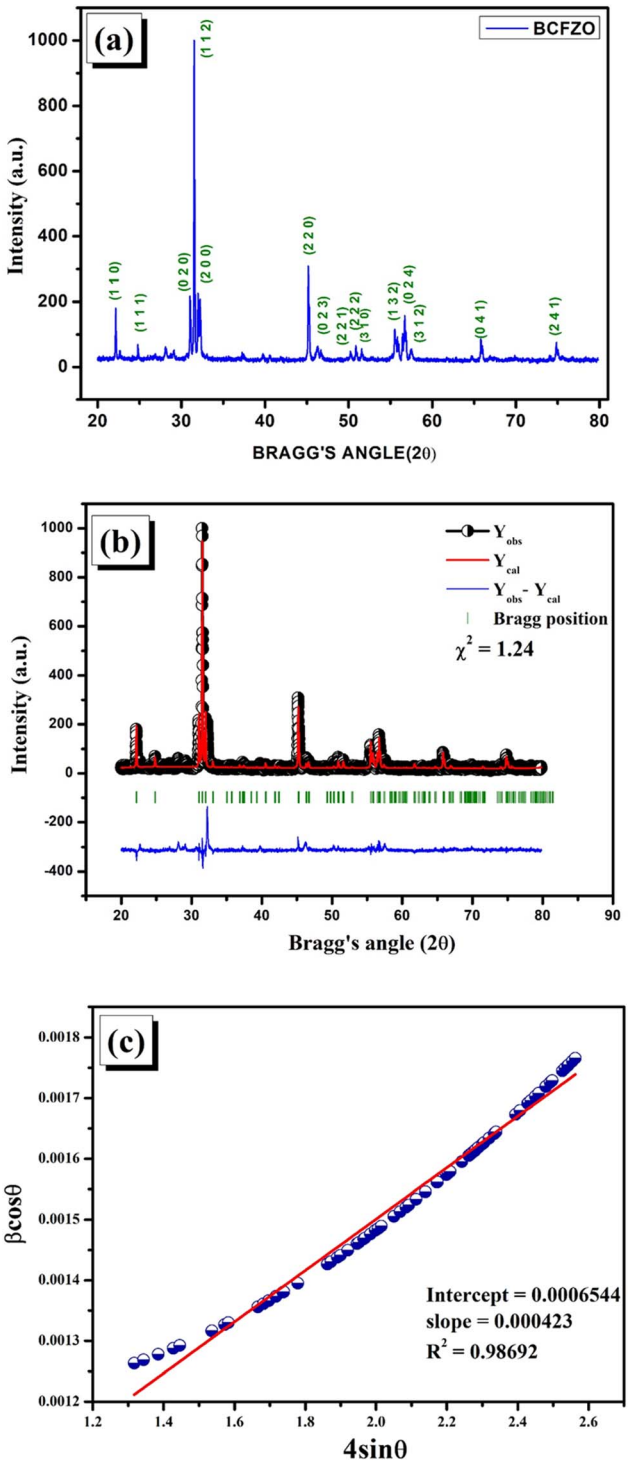

Fig. 1 (a) Indexed X-ray diffraction pattern of $Bi_{0.5}Ca_{1.5}Fe_{0.5}Zr_{1.5}O_6$. (b) Rietveld refinement analysis of $Bi_{0.5}Ca_{1.5}Fe_{0.5}Zr_{1.5}O_6$. (c) W–H plot for *Pcmn* phase.

$Bi_{0.5}Ca_{1.5}Fe_{0.5}Zr_{1.5}O_6$ (BCFZO) at room temperature, highlighting the upward trend of Bragg's angle. The pronounced peaks observed in the X-ray diffraction profile clearly indicate the high level of crystallinity present in the pelletized sample, suggesting a well-organized arrangement of ions within the crystal lattice. The pattern of intensity is predominantly oriented leading to the formation of an orthorhombic structure over a significant range of Bragg's angles (20°–80°).

The minimal occurrence of impurity peaks validates the production of a predominantly pure form of $Bi_{0.5}Ca_{1.5}Fe_{0.5}Zr_{1.5}O_6$. The creation of the orthorhombic phase rather than the basic rhombohedral phase of $BiFeO_3$-based compounds may be due to the presence of Ca^{2+} ions present at the larger cationic site *i.e.*, A-site.[24] Goldschmidt's tolerance factor expression serves as a reliable method for evaluating the firmness of perovskite crystalline structures by taking into account the ionic size of the individual elements. The tolerance factor associated with the double perovskite oxides structure is varied upon the cationic radii of the A and B sites alongside the radius of oxygen, and it can be measured numerically in the following manner:[25]

$$t = \frac{\left(\frac{r_A + r_{A'}}{2}\right) + r_O}{\sqrt{2}\left[\left(\frac{r_B + r_{B'}}{2}\right) + r_O\right]} \quad (2)$$

For the oxide double perovskite material that has been produced, the anionic radius of O^{2-} is recorded at 135 pm. On the other hand, the ionic radii associated with the smaller cationic site exhibit variation *i.e.*, the B-site, Fe^{3+}, and Zr^{4+}, are 63 pm and 79 pm, respectively. The radii for Ca^{2+} and Bi^{3+}ions are determined to be 99 pm and 103 pm, respectively. The atomic radii data are collected from the "Database Ionic Radii by the Atomistic Simulation Group webpage. With $T = 1$, the optimal perovskite compounds take on a cubic, densely packed form. When the ionic radii ratio is not at the optimal value ($T \neq 1$), crystal distortions and geometric strain occur.[26] The non-cubic arrangement of the given perovskite is indicated by the estimated tolerance factor *i.e.*, 0.85.[27] As the tolerance factor is less than but close to 1, the structure is assumed to be a distorted form of cubic arrangements. Given that all the reviews indicated a consistent crystal structure for the specified oxide double perovskite materials, the XRD data was modified and aligned under the premise of orthorhombic crystal symmetry.

The Full Prof refinement software is implemented to execute Rietveld refinement in order to effectively comprehend the phase structure, the elemental positions, lattice arrangements *etc.* The graphical representation displayed in Fig. 1(b), explicitly demonstrates the findings.

The peaks found in the graphical representation of intensity are the most crucial Rietveld refinement parameters since they determine the crystallite size, flaws, detector resolution, stress/strain, and (h k l) indexing. Pseudo-Voigt, the linear integral combination of the Lorentzian and the Gaussian peak function,[28,29] was adopted as the peak function in order to execute the Rietveld refinement. The results from the XRD measurements suggested a configuration that is stable and exhibits a well-organized structure of ions within an orthorhombic symmetric phase, specifically characterized by the (*Pcmn*) space group. Table 1 presents the optimized atomic positions of the constituent ions for the specified phase. The reliability factors presented in Table 2 validate the accuracy of the study methodologies utilized. The augmented cell parameter specifications for the orthorhombic structure are outlined in Table 2. Lower goodness of fit (χ^2), *i.e.*, 1.24, and the small amount of error detected for each parameter show how precise the refining process was. Atoms in the lattice that are at low temperatures and vibrate uniformly in all directions are mediated by the isotropic thermal displacement factor (β) whereas at higher temperatures, anisotropic displacement parameters are required. The thermal effect causes the atom to become less stationary and vibrate around its equilibrium site, which lowers the scattering efficiency. This is determined by the formula $\exp(-\beta \sin^2\theta/\lambda^2)$, which states that the β (thermal displacement factor) decreases as the angle increases. The isotropic thermally mediated displacement factor for all the constituted atoms is given in Table 1. X-ray diffraction pattern of $Bi_{0.5}Ca_{1.5}Fe_{0.5}Zr_{1.5}O_6$ that has been indexed is illustrated in Fig. 1(a).

Table 1 Atomic position and Wycoff position of the given material refined in *Pbnm* phase

	Phase:*Pbnm*			
	Atomic positions			
Atoms	*x*	*y*	*z*	Wyckoff positions
Ca	0.01233	0.96239	0.25	4c
Bi	0.01233	0.96239	0.25	4c
Fe	0	0.5	0	4b
Zr	0	0.5	0	4b
O1	0.75687	0.71966	0.25	4c
O2	0.60228	0.39166	0.97336	8d

The study of the Williamson–Hall curve is plotted to determine the crystalline size and lattice strain linked to the particular arrangement of the crystal, utilizing an updated form of Debye–Scherrer's equation. The Debye–Scherrer equation[21–23] presented below is instrumental in determining the average size of crystalline particles (D).

$$D = \frac{k\lambda}{\beta_{hkl}\cos\theta} \quad (3)$$

Table 2 Refined cell parameters, angles, and reliability factors

Parameters		Phase-1: *Pbnm*
Cell parameters	*a* (Å)	5.590397 ± 0.000263
	b (Å)	5.757947 ± 0.000269
	c (Å)	8.017344 ± 0.000369
Cell angles	α	90
	β	90
	γ	90
Reliability factors	R_p	14.61
	R_{wp}	11.99
	R_{exp}	10.76
	χ^2	1.24

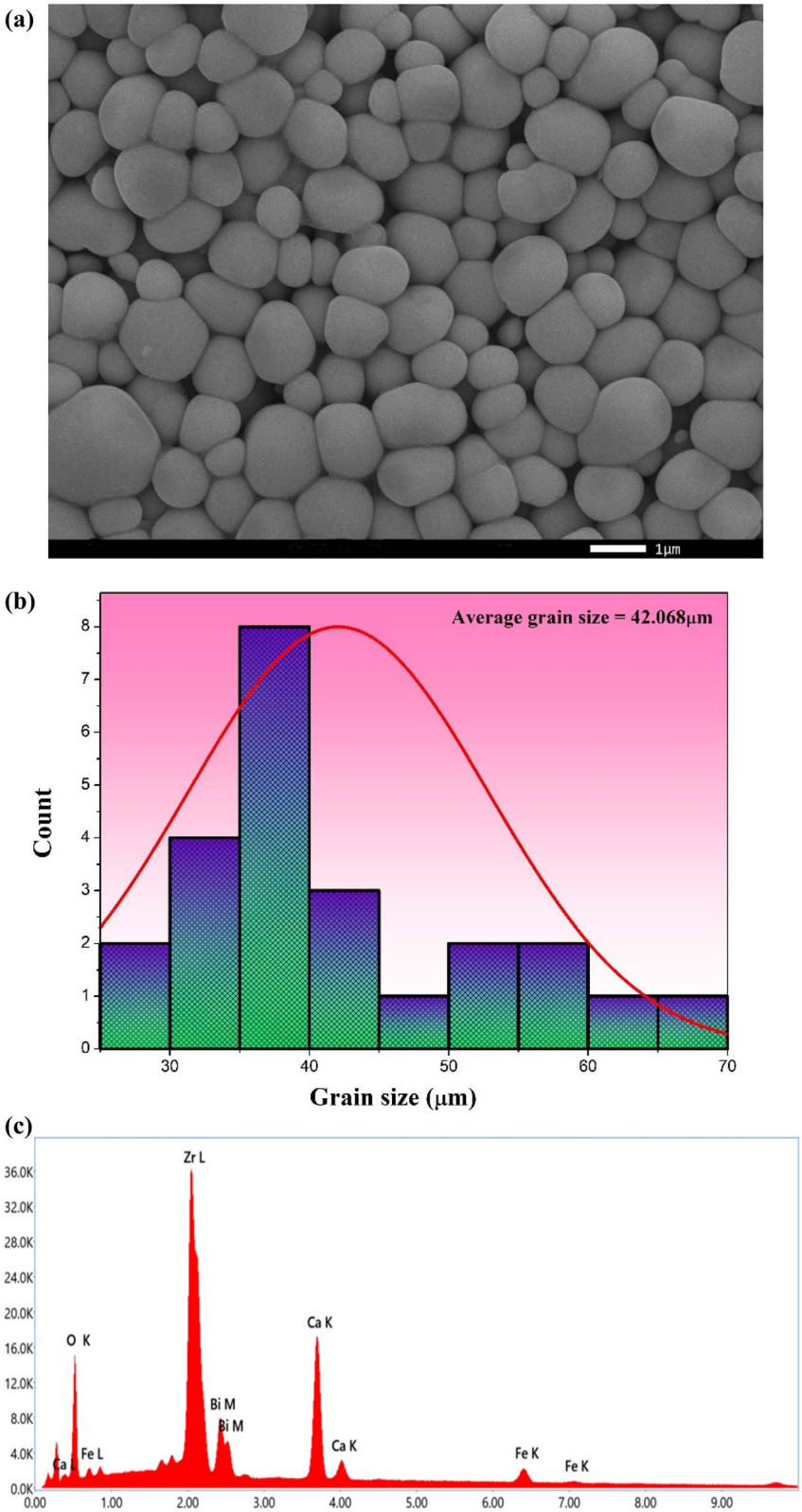

Fig. 2 (a) Microstructural analysis through FESEM micrograph of BCFZO. (b) Histogram mapping for the grain size of the sample. (c) Surface elemental composition by energy dispersive X-ray Spectroscopy.

Eqn (3) can be expressed by considering both the 'β' and the 'ε',[30,31] where 'β' is the full-width half maxima (FWHM) and 'ε' is the lattice strain.

$$\beta \cos \theta = 4\varepsilon \sin \theta + \frac{k\lambda}{D} \quad (4)$$

The shape factor $k = 0.89$ has been established. Fig. 1(c) exhibits the W–H curve for the experimental phase of the freshly created sample, which offers an abundance of information. In the *Pbnm* phase, the data that best fits the model has an R^2 value of 0.98692. The crystalline size, as determined from Fig. 1(c), is measured at 209.52 nm. The lattice strain (indicated by the slope) for the orthorhombic phase present in the prepared perovskite is 0.000432, which implies that the bonds are distorted.

3.1.2 Investigation of microstructural details using field emission scanning electron microscope (FESEM). A surface characterized by a uniform arrangement of microparticles, which are closely packed and exhibit similar sizes and shapes, specifically homogeneously distributed grains with distinct grain boundaries of $Bi_{0.5}Ca_{1.5}Fe_{0.5}Zr_{1.5}O_6$, as demonstrated by the FESEM micrograph, is utilized to examine the grain distribution on the surface, as illustrated in Fig. 2(a).

The emergence of the polycrystalline structure at varying growth rates has been attributed to the slight variation in grain sizes and dimensions.[32] The histogram projection of the grain sizes analyzed using ImageJ software is shown in Fig. 2(b). By applying a Gaussian fit to the histogram statistics, we determined that the average particle size is 42.068 μm.

3.1.3 Exploration of elemental composition by energy dispersive spectroscopy (EDS). Energy dispersive spectroscopy (EDS) technique is used to confirm the presence of the required elements in the manufactured oxide perovskite. This is shown in Fig. 2(c). Additionally, the absence of impurity peaks further confirms the sample's purity.

3.1.4 Fourier Transform Infrared Spectroscopy (FTIR) analysis. A thorough insight into the absorption and emission spectra of material has been enlightened by implementing Fourier Transform Infrared Spectroscopy *i.e.*, FTIR spectroscopic data obtained as intensified peaks while passing the newly prepared material through the intense wavelength of infrared light. Investigating the peaks at different wavenumbers helps us make important scientific discoveries by providing us with significant bits of information on the properties and response of the covalent bonds at the molecular level. Fig. 3 exhibits the FTIR statistics for the as-prepared oxide perovskite material concerning the transmittance (T) that varies from 250 cm^{-1} to 3000 cm^{-1}.

The particular type of lattice vibration is associated with vibrations in the 850–400 cm^{-1} range 22. In double-ordered perovskite materials, the transmission bands at 814, 946, and 1339 cm^{-1} can be pursued to identify the presence of perovskite phases.[33] The notable peaks at 503, 519532, 546, 558, and 569 cm^{-1} may be attributed to the anti-symmetric oscillations of transition metal oxide octahedra *i.e.*, ZrO_6 and FeO_6 present at B-cationic site[34] or the symmetrical stretching of BiO_6 present at the larger cationic site.[35,36] It is more accessible to the researchers to precisely identify and evaluate certain materials since the oscillation of phonons is linked to specific wavenumber ranges. This demonstrates the special characteristics of the material's composition and vibrational characteristics.[37] The findings suggest that the stretching vibrations detected in the specimen at 814 and 946 cm^{-1} can be linked to Fe–O octahedral bonds. Furthermore, it was shown that the overtones associated with robust C–O bond vibrations, which are linked to the vibration of the carbonate ion (CO^{2-}), were the main contributors to the peaks detected at 1339 cm^{-1} and 1983 cm^{-1}.[37]

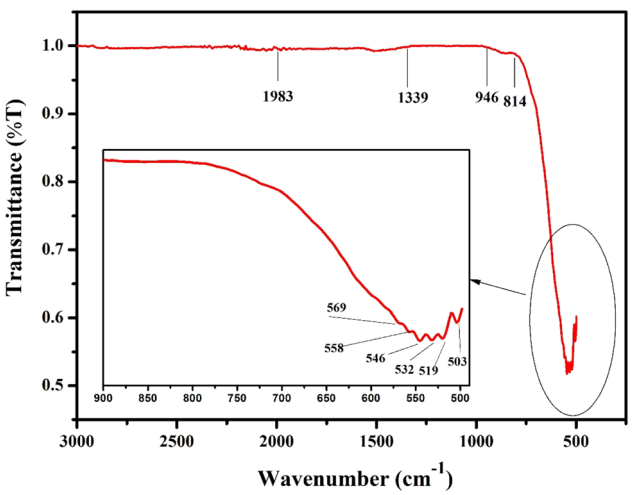

Fig. 3 FTIR pattern of the prepared sample.

4. Optical property analysis

Analysis using UV-vis spectroscopy provides precise information about the responsiveness of the sample to the electromagnetic (EM) radiation that occurs in the range of ultraviolet -visible spectrum. It facilitates its use in a variety of optoelectronic devices.[38] The absorption spectra associated with the desired sample BCFZO can be observed in Fig. 4(a) and (b). The movement of charged ions from the highest-filled orbital (2p) of oxygen to the half-filled orbitals (3d) of iron may be the reason for the improved absorbance of the double perovskite in the 200–700 nm range.[39–41] The cutoff absorption wavelength of sunlight is roughly 570 nm, and the BCFZO sample exhibits substantial absorption in the ultraviolet light area, demonstrating that the photocatalytic activity of BCFZO has a specific visible light response.[42] Specifically, classical Tauc's relation is employed to evaluate the optical energy bandgap (E_g) for BCFZO, which is expressed using the absorption coefficient (α) determined by the Kubelka–Munk function, the photon energy ($h\nu$) & the electronic transition index (n) as the following equation:

$$\alpha h\nu = A(h\nu - E_g)^n \quad (5)$$

The suggested values of $n = 1/2$ for the direct transition and $n = 2$ for the indirect band transition depending upon the type of electronic transition between the energy bands. Many

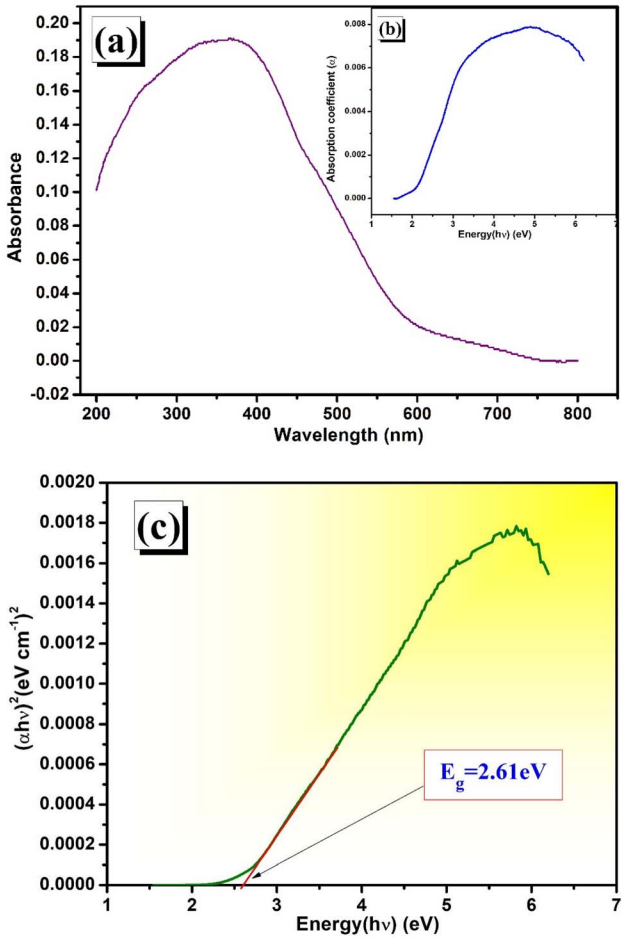

Fig. 4 (a) and (b): UV-vis spectroscopy (a) absorbance *vs.* wavelength, (b) absorption coefficient *vs.* photon energy. (c) The calculated band gaps of the synthesized BCFZO using UV-vis absorption spectrum.

researchers have claimed that BFO is a direct bandgap semiconductor.[38,43,44] Based on that, we prioritized the direct electronic transition to obtain the corresponding direct energy bandgap obtained by extrapolating the linear zone of this plot to $(\alpha h\nu)^2 = 0$ (towards the *x*-axis) as shown in Fig. 4(c) It is calculated that the sample's bandgap energy value is 2.61 eV.[23] Similarly, Fig. 5a and b depicts the reflectance *vs.* engery and reflection coefficient *vs.* energy respectively. The Kubelka–Munk function can also be used to obtain the value of E_g from diffused reflection spectroscopy (DRS):

$$(F(R)h\nu)^{1/n} = A(h\nu - E_g)^n \quad (6)$$

where the $F(R)$ is represented in terms of reflectance (R) as

$$F(R) = \frac{(1-R)^2}{2R} \quad (7)$$

Directly permitted transitions are represented by the index $n = \frac{1}{2}$, whereas indirectly permitted ion transitions are represented by $n = 2$. The reflectance bandgap energy derived by extrapolating the linear section of the $(F(R)h\nu)^2$ *vs.* $h\nu$ curve (Fig. 5) *i.e.*, $E_g = 2.69$ eV, is approaching the band gap energy obtained in the absorbance plot which suggests the utilization of this oxide double perovskite material for photocatalysis.[45,46] The significantly larger particle size and an increase in oxygen vacancies in the sample under study may be the basic reason behind the lower energy band gap value. Depending on the doping or the presence of defects *i.e.*, oxygen vacancies, dielectric perovskites can have either a metallic or semiconducting nature. N-type semiconductors with the Fermi level close to the bottom of the conduction band are produced by oxygen vacancies acting as donor sources. Although the band gap narrows in both situations, we think that samples doped with iron should have a smaller band gap because of the role that iron orbitals play in the valence and conduction bands. Because of their empty d-shell electrons and octahedral distortions, the transition metal cations Zr/Fe at B′ and B″ sites in the double perovskite can account for the observed optical band gap energy. This suggests that the produced material may find application in the solar device industry.[47] Energy gap calculations can be exploited to establish the refractive index (n) of the semiconductor, a crucial optical characteristic that may be employed to examine the potential use of the material in integrated optical systems. The Dimitrov and Sakka relation is used to calculate "n" using the direct band gap energy E_g[48] as follows:

$$\frac{n^2-1}{n^2+2} = 1 - \sqrt{\frac{E_g}{20}} \quad (8)$$

The computed value of n is around 2.51. In most cases, photonic nanojets (PNJs) only happen when the underlying material and microparticle have refractive indices (n) that differ by less than 2; however, Guoqiang Gu and colleagues suggested a way to go beyond the refractive index upper restriction and produce ultra-narrow PNJs.[49] This suggests that the high value of refractive index obtained for our product might be useful for optoelectronic applications.

5. Dielectric property study

An equation that defines the dielectric properties of a material can express the complex dielectric function in relation to an external field is given by:

$$\varepsilon = \varepsilon' + \varepsilon'' \quad (9)$$

ε' is the real component and ε'' is the imaginary component of the dielectric constant. ε' is applied field-dependent component while the imaginary part represents the energy dissipation. $\varepsilon''/\varepsilon'$ (=tan δ) represents the dissipation factor, and $\varepsilon'' = \varepsilon\varepsilon +$ tan δ represents the dissipation term. The phase shift brought on by an electric current is best represented by the symbol "δ".[50]

5.1. Frequency-dependent of dielectric constant and dielectric loss

The variations in dielectric constant and dielectric loss as a function of frequency are depicted in Fig. 6(a) and (b) respectively for $Ca_{1.5}Bi_{0.5}Fe_{1.5}Zr_{0.5}O_6$.

Measurements of the dielectric constant were conducted at temperatures between 250 °C and 325 °C, with intervals of 30 °

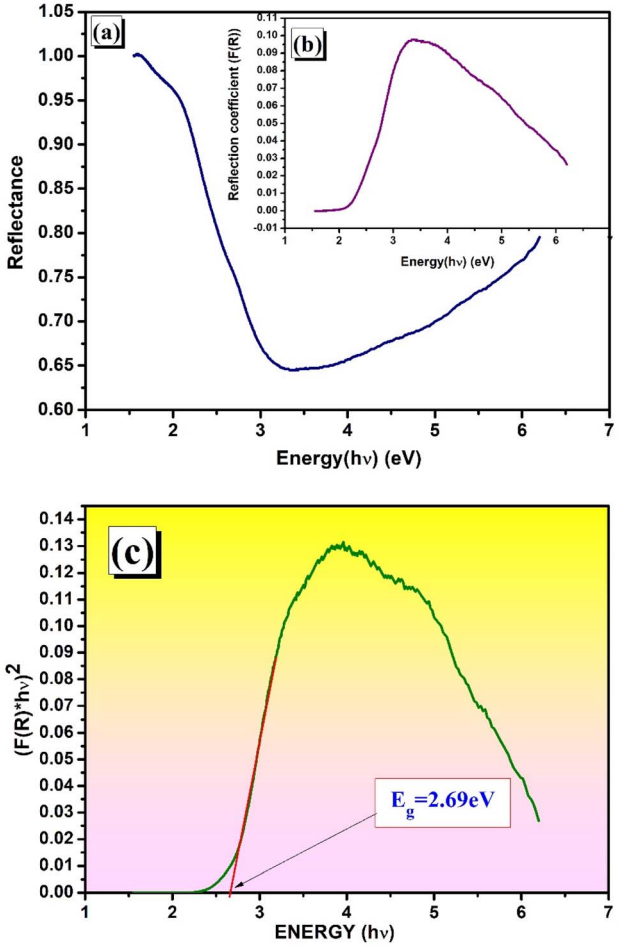

Fig. 5 (a) and (b): Typical UV-visible reflection spectra of synthesized BCFZO (a) reflectance *vs.* photon energy, (b) reflection coefficient *vs.* photon energy. (c) The calculated band gaps of the synthesized BCFZO using UV-vis reflection spectrum $(F(R)*h\nu)^2$ *vs.* photon energy.

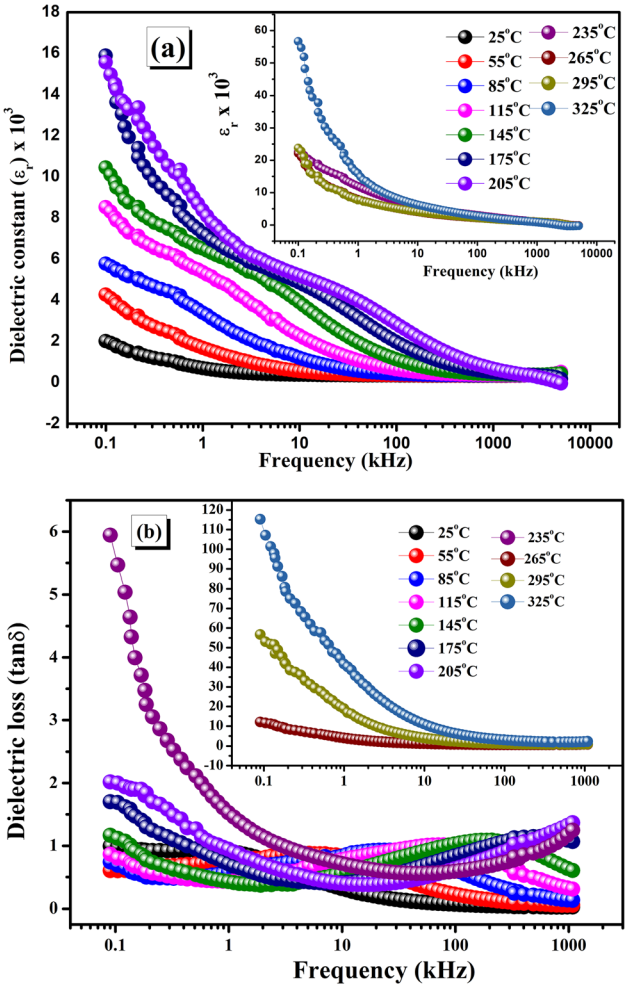

Fig. 6 (a) Frequency-dependent dielectric constant (ε_r) at different temperatures. (b) Frequency-dependent dielectric loss at various temperature.

C, and over a frequency range extending from 100 Hz to 1 MHz, reflecting the effects of different polarizability as determined by the applied field. As the frequency increases, ε_r and tan δ become evident prior to the signal indicating dipolar orientation switching. This phenomenon occurs due to the absence of certain polarising variables in the higher frequency range, while ionic, electronic, and dipolar polarisation exhibit the greatest polarisability in the low-frequency domain. The results of Maxwell–Wagner's experiment indicate that multiple polarization effects,[44] which create a nearly linear ambiguity in the high-frequency spectrum, may account for the high dielectric values noted at lower frequencies. The pronounced decrease, indicative of dipolar relaxation processes, is additionally corroborated by linear representations of graphs at elevated frequencies.[51] Space charge polarization arises from the presence of grains situated in the insulating matrix, resulting in a notable polarization effect that has been recognized for enhancing the performance of insulating materials. Local charges build up around an electric field, offering significantly higher efficiency that can be used effectively in a wider range of electronic devices.[52–54] The dielectric characteristics of the intended product indicate that dielectric loss increases with rising frequency. At lower frequencies, the predominant factor contributing to the high loss is the surface charge effect, whereas the significant reduction in dielectric loss (tan δ) is attributed to the dipolar relaxation process.[55] At higher frequencies, the applied electric field oscillates, causing an overall relaxation effect that causes the space charges to react quickly.[56] BCFZO demonstrates remarkable dielectric properties, characterized by a great value of ε_r(=2012.54) and a minimal tan δ (=0.99521) at room temperature at 100 Hz.

5.2. Temperature-dependent of dielectric constant and dielectric loss

The variation of dielectric constants (ε_r) in relation to dielectric losses (tan δ) is depicted in Fig. 7 at different temperatures ranging from 25 °C to 250 °C. It also explores the variation in the above mentioned parameters at various frequencies, including 100 Hz, 1 kHz, 10 kHz, 100 kHz, and 1 MHz, in sections (a) and (b). Observations have indicated that the dielectric properties, including tangent loss and relative

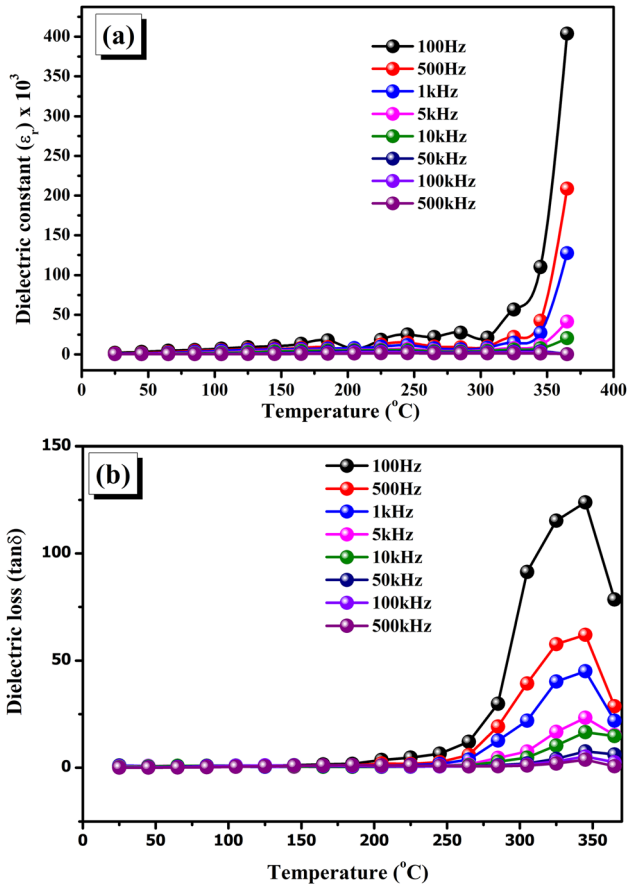

Fig. 7 (a) Temperature-dependent dielectric constant. (b) Temperature-dependent tangent loss.

permittivity, exhibited an upward trend in relation to temperature across all frequencies, which can be attributed to different polarization mechanisms, especially dipolar polarization. At temperatures above 250 °C, a notable increase in ε_r and tan δ at a frequency of 100 Hz may suggest the presence of thermally activated oxygen vacancies and charges. Because it is difficult to align dipoles in the low-temperature state and there is insufficient thermal energy for the migration of B-site cations, the dielectric constant inclined to be smaller and more stable at lower temperatures. An increase in temperature causes the dielectric constant to rise, a phenomenon linked to the enhanced mobility of charge carriers that are influenced by thermal agitation. Furthermore, the notable tangent loss detected could be associated with the polaron hopping mechanism, which is triggered by lattice vibrations within sample exposed to elevated temperatures.[57,58]

6. Study of complex impedance spectroscopy (CIS)

Analyzing CIS is vital for interpreting the transport and relaxation dynamics of perovskite materials. During this detailed procedure, the specimen is methodically exposed to alternating field to investigate the alignment of the mobility of charge carriers and electric dipoles. An advanced LCR analyzer, carefully monitored by a computer, records the data to ensure accurate and precise measurements across a broad spectrum of frequencies, spanning from 100 Hz to 1 MHz, considering different temperature conditions. The complex impedance $Z^*(\omega)$ of a material, which varies with the angular frequency (ω), can be defined using its real and imaginary part of complex impedance.

$$Z^*(\omega) = Z'(\omega) - jZ''(\omega) \quad (10)$$

Three factors involving polarisation interact across different frequency ranges, influencing the semi-circular shapes observed in the complex impedance spectra which include the polarisation created between grains, polarisation at grain boundaries and electrode polarisation.[59,60] The real component (Z') and imaginary part (Z'') of the impedance with varying frequency can be expressed as,

$$Z' = R/(\omega^2\tau^2);\ Z'' = \omega R/(\omega^2\tau^2) \quad (11)$$

In this context, we use the symbol τ to represent the relaxation time, encompassing the measured values of resistance (R) and capacitance (C) through the equation $\tau = RC$, while ω is used to represent the angular frequency. In this case, the imaginary part of the impedance corresponds to the reactive part, whereas the real part correlates to the resistive part. Fig. 8(a) and (b) showcase the plotted frequency-dependent real and imaginary impedance across different temperature ranges. A more distinct polarisation within the ceramic occurs at lower frequencies, as shown by a higher value. The reduction in resistances takes place through grain–grain interaction, grain boundary, and electrode interface with the sudden diminution of Z' and Z'' with frequency and temperature.[61–63] The decline in Z'' value as the temperature rises, demonstrating high conductivity of the fractionally substituted double perovskite sample. This behaviour occurs because the relaxation phenomena caused by immobile species at low temperature range, whereas at high temperatures, vacancies and crystal defects contributes to the same. The synthesized specimen displays semiconducting behavior, as evidenced by the negative temperature coefficient of resistance (NTCR), which is associated with a reduction in impedance values across different temperatures.

6.1. Nyquist plot

Impedance analysis is a compelling and non-destructive technique for examining how ceramic materials respond electrically to AC impulses. Distinct charge hopping processes resulting from inhomogeneous variations in conduction caused by the grain and grain border in ferrite based perovskite systems. The Nyquist plot or compound complex impedance spectra (CIS) is recorded to confirm the significance of the grain and grain boundary to the observed dielectric and transport/conductivity properties. A Nyquist plot displaying the graph between Z' and Z'' is represented in Fig. 8(c-1 and c-2) to investigate the performance of the ceramic compound. As a result, the effects of the grain and grain boundary effects on the sample may be

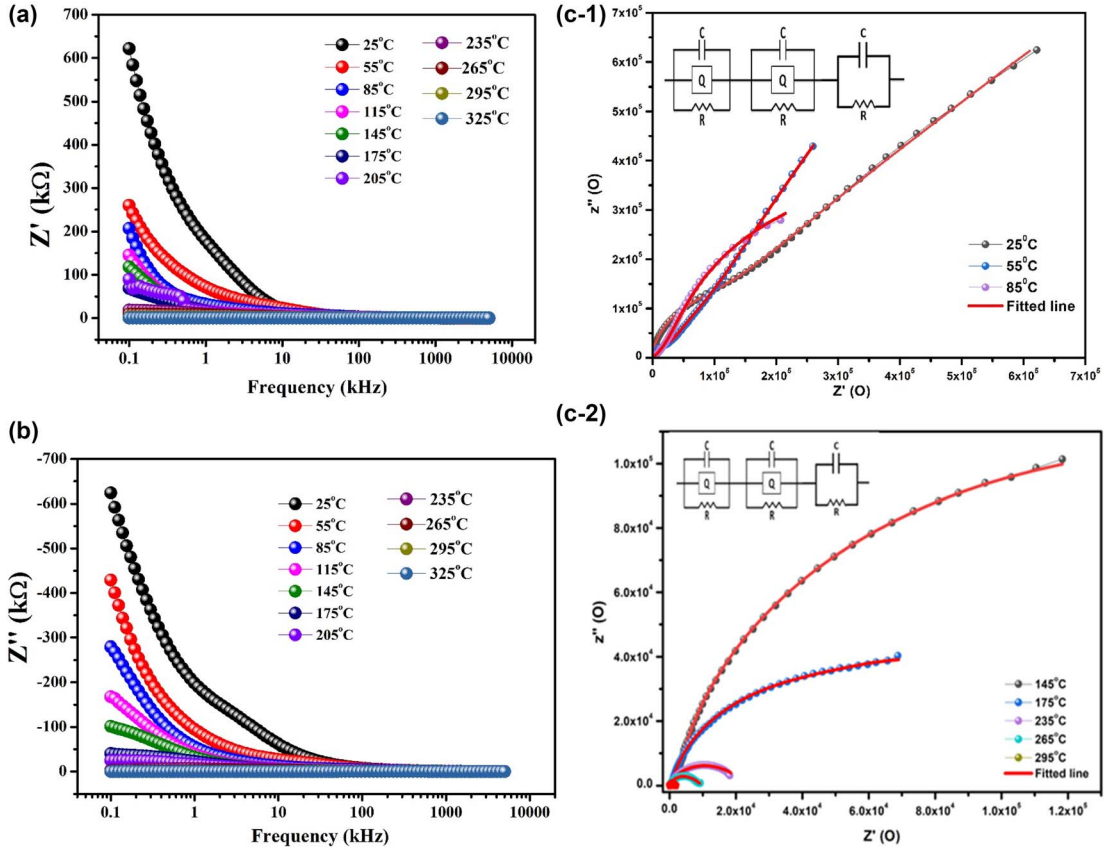

Fig. 8 (a) Frequency varying Real impedance (Z'). (b) Frequency varying imaginary impedance (Z'') with different temperature. (c-1) $Z'-Z''$ (impedance Nyquist plot) at lower temperature. (c-2) $Z'-Z''$ (impedance Nyquist plot) at higher temperature.

adequately comprehended at various temperatures in the frequency range of 100 Hz to 1 MHz. The Nyquist plot ($Z' \sim Z''$) illustrates the phenomenon with the highest resistance. Both the scattered nature of electromagnetic waves and fluctuations in particle size[64,65] can be accountable for the observed depressed semicircles, which are suggestive of dispersion in relaxation time. In the Nyquist plot, the intrinsic and extrinsic grain boundary effects are manifested as a series of semicircular arcs. The relaxation processes (Debye or Non-Debye) of the product are specified by the semicircular nature (perfect or depressed). The Debye type relaxation mechanism is specified by a perfect semicircular arc, or one with the centre on the real Z-axis; the non-Debye relaxation process is indicated by a depressed semicircular arc, or one with the centre below the real Z-axis. This statistical approach compared the experimental impedance data with the impedance of the stimulated electrical circuit with the ideal resistor (R) and capacitor (C). The influence of the bulk grain was demonstrated by the semi-circular arcs aligning with a serially connected RQC, RQC, and RC (Q = constant phase element) from 25 °C to 295 °C.[66] Both the grain and grain barrier effects were observed at all the allowed temperatures. The incorporation of Q in the circuit signifies the non-Debye-type relaxation processes. The decreasing frequency is the result of both grain and grain boundary contributions over temperature,[65–67] which causes the semicircular arc to gradually decrease. The charge transport channel in the intra-grain and grain boundary regions is efficiently stimulated by thermal activation.[68,69]

7. Complex modulus spectroscopy

Electric modulus spectroscopy which has the ability to eliminate the electrode polarisation effect arising while measuring impedance is a crucial method for understanding conductivity and relaxation mechanisms.[69] Electric modulus in terms of real modulus (M') and imaginary modulus (M'') is represented as,

$$M = \frac{1}{\varepsilon^*} = M' + jM'' \quad (12)$$

Fig. 9(a) and (b) depict the variation of M' and M'' with frequency. A decrease in M' at lower frequencies, along with an increase in dispersion at higher frequency ranges can be ascribed to the restricted charge carrier's mobility within a short-range context. M' diminishes with the decreases of frequency. The absence of restoring forces has an effect on mobility here, which arises from the application of the electric field.[68,70] Examining the M' curves reveals a flattened S-shaped decline that eventually approaches zero, indicating that there is no electrode polarisation effect. The M' plot continuously rises with frequency and integrates in the high-frequency region, confirming the release of space charge polarisation.

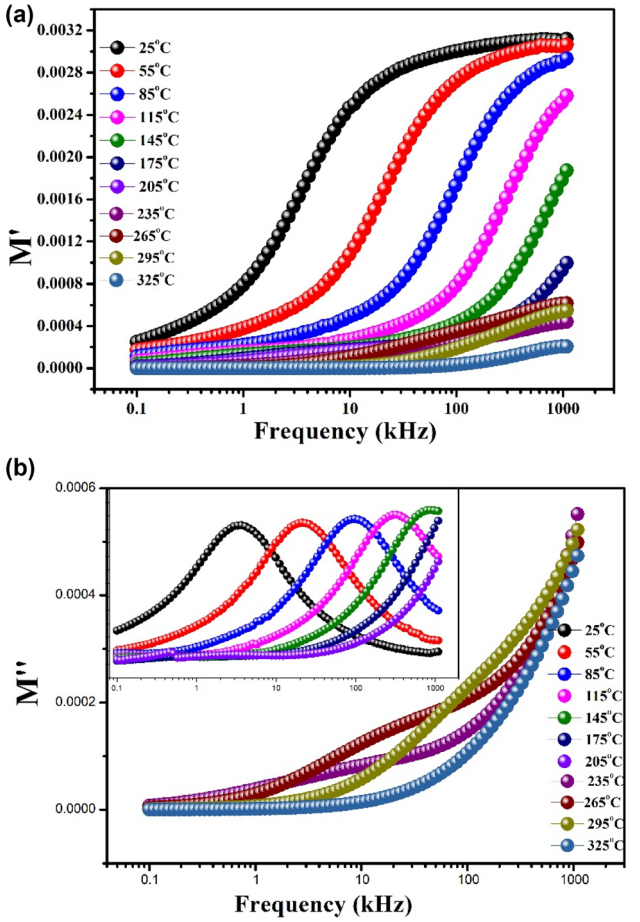

Fig. 9 (a) Variation of real modulus (M') with frequency at different temperatures. (b) Variation of imaginary modulus (M'') with frequency at different temperatures.

The findings of dielectric and impedance experiments provide strong evidence for this nature. It is important to highlight that as temperatures rise, the M' values for all the temperatures consistently decline until they converge at the high frequency region, which is solely due to the lack of electrode-polarization at this.[67] Thus, the conduction process is mediated by the short-distance mobility of charge carriers. The notable movement of the M'' peaks towards elevated frequencies with the increase in temperature suggests that the relaxation process is occurring in the identified perovskite sample and is influenced by temperature, with charge carriers primarily confined to specific potential wells.[71,72] With the rise in temperature, a significant increase in the peak height of the M' *versus* frequency plots was observed. This finding implies that ferroelectric materials frequently show a decrease in capacitance as the temperature rises.[72]

8. Conductivity formalism of the material

Understanding numerous physical features, especially the mechanical, optical, and dielectric performance of the dielectric material in anticipation of electric impulses, relies on assessing their electrical conductivity. Effective electrical conduction in dielectric arises from the systematic mobility of charged particles in response to the exerted electric field.[73] In the materials, conductivity usually occurs through the hopping interactions between donor and acceptor components, which is influenced by the temperature. Due to the poor portability of the constituent ions, this process is essential for effective conduction. An extrinsic alternating current field considerably influences the conductivity process in a dielectric sample. In this instance, one of the main factors increasing the total conductivity is diffusion among the weakly bound ions, or mobile charge carriers.[33,74] Several techniques are frequently used to ascertain the perovskites' AC conductivity properties, especially in relation to temperature-dependent fluctuations. Mechanisms like overlapping large polaron tunnelling (OLPT), non-overlapping small polaron tunnelling (NSPT), quantum mechanical tunnelling (QMT), variable range hopping (VRH), and small polaron hopping (SPH) contribute to a deeper understanding of the complex interactions present in oxide double perovskite materials at various temperatures.

8.1 Exploration of frequency-dependent AC conductivity(σ_{ac})

AC conductivity (σ_{ac}) can be defined in relation to angular frequency (ω), relative dielectric permittivity (ε_r), absolute permittivity (ε_o), and the tangent loss (tan δ) as follows:

$$\sigma_{ac} = \omega\varepsilon_r\varepsilon_o \tan \delta \quad (13)$$

The relationship of electrical conductivity (σ_{ac}) with the frequency of the external field is represented in Fig. 10(a) for temperatures spanning from 250 °C to 295 °C. The significant increase in the σ_{ac} with increasing frequency and temperature highlights the conduction mechanisms that originate from the temperature-dependent hopping interactions among the charged particle. The graphical depiction clearly illustrates that the σ_{ac} display a linear relationship in frequency dependence at all temperatures observed in the low-frequency domain. Which suggests a reliable and well-defined connection between conductivity and frequency.

Both the existence of interfacial or space charge polarisation and disruptions in the cation arrangement within neighbouring sites can be responsible for the increase in AC conductivity that is seen at lower frequencies. The enhanced electrical conductivity is supported by these elements.[37,75] The curves representing AC conductivity show a unique pattern at higher frequencies throughout all temperature ranges. This nature is characterized by dispersion and saturation, resulting from the hopping behavior of electrons at higher frequencies.[76] The generation of polaron entities occurs at sites adjacent to the $\sigma_{ac} \sim f$ graphs, characterized by a plateau and dispersion,[67] as a consequence of localized charge carriers participating in the conduction mechanism.

The plateau area at lower frequencies signifies the existence of diverse range of σ_{dc}, whereas at higher frequencies the dispersion area demonstrates localized σ_{ac}. For a clear understanding into these regions, the Jonscher Power law equation

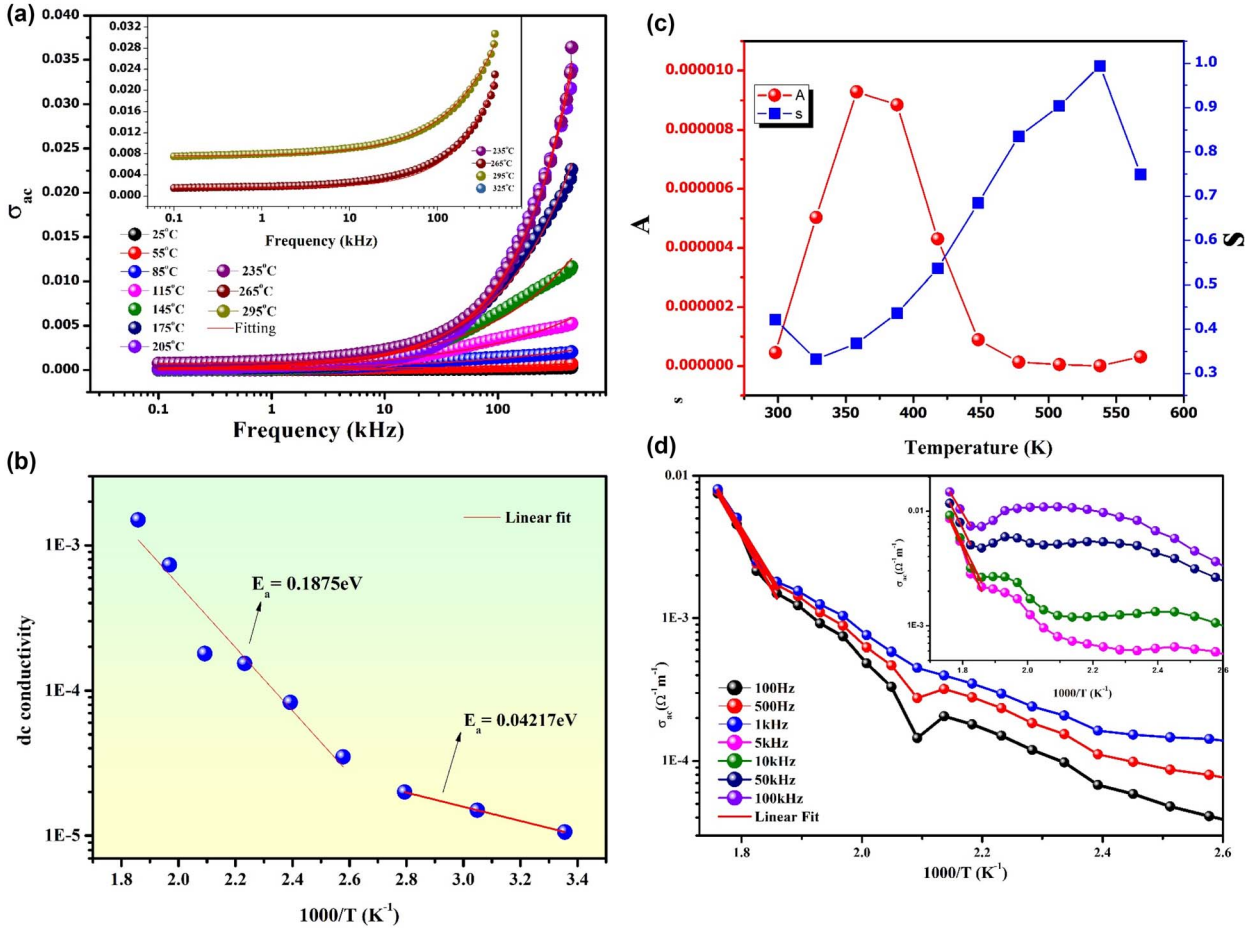

Fig. 10 (a) AC conductivity as a function of frequency at various temperatures with Jonscher Power law fitting. (b) DC conductivity *vs.* 1000/*T*. (c) Temperature-dependent s and A. (d) AC conductivity *vs.* 1000/*T*.

pertaining to σ_{dc} and angular frequency (ω) can be expressed in the following manner:

$$\sigma_{ac} = \sigma_{dc} + A\omega^{s} \quad (14)$$

where, '*s*' is the power law exponent and '*A*' is the pre-exponential constant. In Fig. 10(a), a graphical illustration fitted to Jonscher's law reveals the σ_{dc}, '*A*', and s' of the material for ranges of frequencies. Fig. 10(b) shows the plot of direct current conductivity against 1000/*T* which demonstrates two linear segments. Arrhenius expression shown below is used to calculate activation energy (E_a) using these;

$$\sigma_{dc} = \sigma_o e^{\frac{-E_a}{k_\beta T}} \quad (15)$$

where k_β and σ_0 stand for the Boltzmann constant and pre-exponential factor, respectively.[57] Two distinct activation energies have been determined using the linearly fitted data: 0.04217 eV for the lower temperature region and 0.1875 eV for the higher temperature region. The intriguing "*s*" and "*A*" phenomena are displayed against temperature in Fig. 10(c). On the other hand, a correlated barrier hopping phenomenon occurs in the conduction process when the value of '*s*' decreases as the temperature rises. Again, it suggests that tiny polaron conduction is the primary mechanism that increases with temperature.[77] It has been shown that for the given material, '*s*' initially decreases, achieves a minimum, and then starts to grow with increasing temperature. Given this trend, the most relevant conduction mechanism is overlapping large polaron tunnelling.[60,78] The explanation for the minimal value of '*s*' and the maximal value of '*A*' at the specified temperature lies in the controlled range of correlation among the charge carriers.[59]

8.2. Exploration of temperature-dependent AC conductivity (σ_{ac})

The σ_{ac} is represented in Fig. 10(d) as a function of inverse temperature, specifically at selected spectrum of frequencies.

At reduced temperatures, the graph reveals a broad spectrum of AC conductivity readings. With the increase in temperature, these values are likely to increase and converge at higher temperature points. The boost in conductivity with temperature signifies the material being studied operates through a hopping mechanism that is influenced by temperature. The rise in σ_{ac} is a result of carriers that are thermally activated.[78] The results imply that the sample possesses a negative temperature coefficient of resistance (NTCR) and exhibits characteristics of

Table 3 Calculated activation energies for different frequencies

Sl. No.	Frequency (kHz)	Activation energy (E_a)
1	0.1	0.64308 eV
2	0.5	0.60423 eV
3	1	0.58356 eV
4	5	0.54504 eV
5	10	0.49675 eV
6	50	0.48990 eV
7	100	0.40058 eV

semiconducting materials. The activation energy associated with the given frequency is illustrated in Table 3, determined by utilizing the Arrhenius equation.

9. The impact of temperature on resistance

The characteristics of the material, specifically its Negative Temperature Coefficient of Resistance (NTCR), allowed for the development of a sensing device called a thermistor, which operates by analyzing the changes in resistance as temperature varies.[79] Thermistors can be categorized into two primary categories: the negative temperature coefficient (NTC) thermistor and the positive temperature coefficient (PTC) thermistor. Based on our current analysis, we show a tendency to favour the NTC thermistor. The variation in resistance from 300 K to 600 K is represented in Fig. 11(a), while Fig. 11(b) illustrates the variation ln R with $1/T$. A complete understanding of the operational principles of a thermistor necessitates the examination of various physical factors, including the thermistor constant (β), activation energy (E_a), and sensitivity index (α). We can gain a deeper insight into the fundamental principles and processes involved[79] by analyzing the mathematical relationships $R_\tau = \alpha\ e^{1/T}$ and $\log\ R = C + 1/T$, where, α and C are constants. The findings from our experiments indicate that a linear correlation between $\log\ R$ and $1/T$ is essential for the proper functioning of the thermistor. The following is the exact formula for determining the thermistor constant (β):

$$\beta = \frac{\ln\left(\frac{R_1}{R_2}\right)}{\left(\frac{1}{T_1} - \frac{1}{T_2}\right)} \quad (16)$$

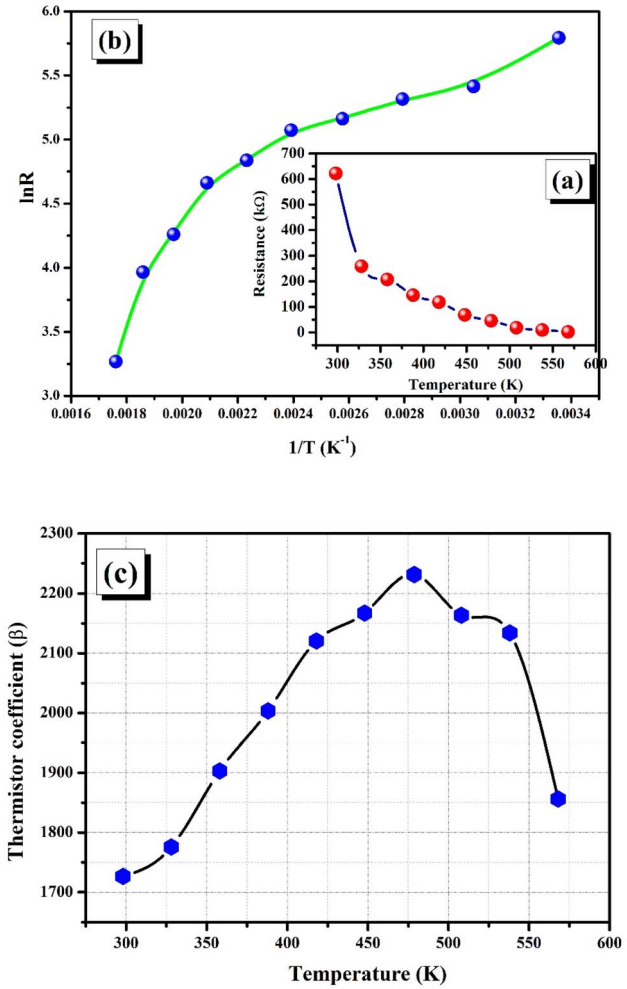

Fig. 11 (a and b): (a) Change in resistance with temperature; (b) ln R *versus* $1/T$ (c) Thermistor constant (β) *vs.* temperature.

Fig. 11(c) demonstrates the relationship between the thermistor coefficient (β) and 'T'. The synthesized double perovskite exhibits negative temperature coefficient (NTC) characteristics, as demonstrated by the increasing connections of 'β' with 'T', which reflects a notable NTC-type thermistor response.[80] This amply demonstrates the value of thermosensor applications. A larger thermistor constant is unquestionably beneficial for the production of NTC-thermistors.

10. Magnetic properties of BCFZO

The scrutiny of the magnetic functionality of the prepared perovskite is emphasised by the simultaneous presence of two ferromagnetic ions, namely Fe and Zr, at the B-site. With the goal of exploring potential utilises of the transition metal substituted oxide perovskite in different industrial sectors, the magnetisation potential of the generated specimen is evaluated using magnetisation with the applied magnetic field. The interaction of simulated electrons between two half-filled orbitals, one half-filled with completely filled, or empty orbitals is governed by the Goodenough-Kanamori rule for 180° super-exchange coupling. This rule helps to balance the magnetic properties of transition metal-substituted perovskite materials.[81,82] The antiferromagnetic characteristics of these materials are determined by the super-exchange interactions between two half-filled overlapping orbitals that are involved in the spin exchange mechanism. The replacement of Zr^{4+} cations at the Fe^{3+} cationic site results in exceptional retention of charge neutrality, which adds two crucial features to Zr-doped $BiFeO_3$ materials. First and foremost, it facilitates the detection of anion site *i.e.*, the oxygen sites. Secondly, Fe^{3+} cations undergo conversion into Fe^{4+} cations. When paired together, the cations Fe^{3+} and Fe^{4+} can exhibit ferromagnetic properties

through enhanced magnetization.[81,83] Fig. 12(a) and fig(b) depicts the hysteresis curves between '*M*' and '*H*' from −15,000 Oe to +15,000 Oe.

Law Approach of Saturation (LAS) is formulated to help understand the magnetic materials more precisely. Different intrinsic properties such as saturation of magnetization, anisotropic constant, and anisotropic fields can be determined using this method with four different formulations, *i.e.*, Akulov Model of LAS, Brown Model, Grosinger, and Néel Model. These models are the modified versions of the most general expression of LAS *i.e.*, the Grossinger equation.[84]

$$M = M_s\left[1 - \frac{a}{H} - \frac{b}{H^2} - \frac{c}{H^3}\right] + \chi H \quad (17)$$

The terms Ms, *a*, *b*, *c*, χ are the denotation of saturation magnetization, inhomogeneity parameter, magnetic anisotropy, and magnetic susceptibility, respectively. The anisotropic parameter b in terms of anisotropic constant (K_1) and anisotropic field (H_a) can be represented as,

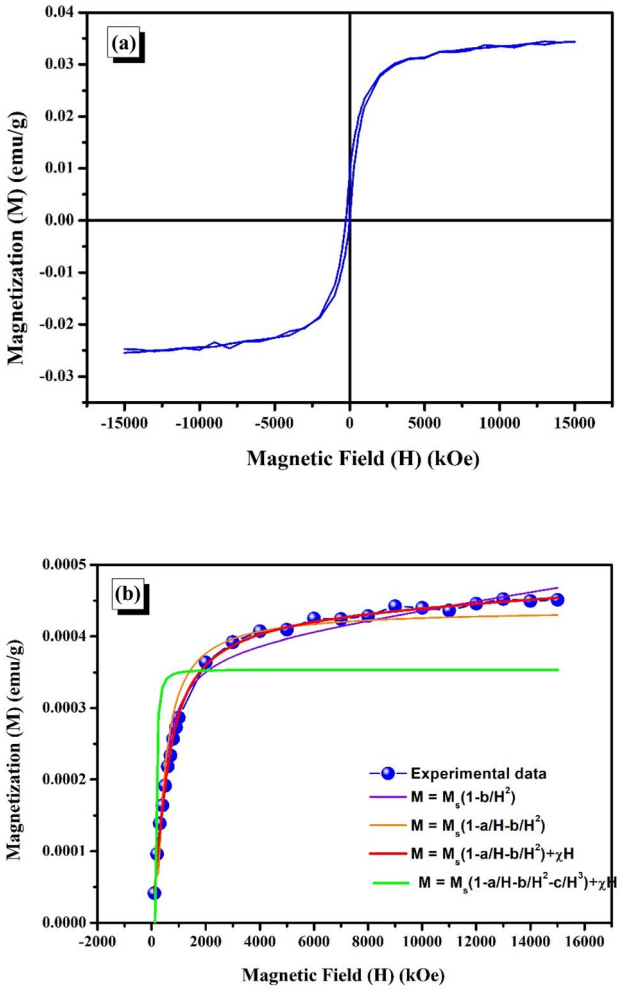

Fig. 12 (a) M–H hysteresis loop and LAS approach of saturation magnetization for the prepared perovskite. (b) M–H hysteresis loop and LAS approach of saturation magnetization for the prepared perovskite.

$$b = \frac{8}{105} X \frac{{K_1}^2}{{M_s}^2} = \frac{2}{105}{H_a}^2 \quad (18)$$

The equation indicates that a positive *b* value can define inherent magnetic characteristics of the desired product, including anisotropy constant and anisotropic field. A positive *b* value suggests that the field adequately provides the computed M_s value. A negative number implies that the applied magnetic field is insufficient for saturation magnetization.[84] One of the most crucial characteristics of magnetic materials for technological applications is magnetic anisotropy. Materials with moderate, low, or high values of magnetic anisotropy are required for certain applications, such as information storage media, permanent magnets, magnetic cores in transformers, and magnetic recording heads.[85] Different Magnetisation Models are tabulated in Table 4, along with the expressions and the calculated parameters obtained after fitting the models individually.

11. *I–V* characteristic study

The relationship of current and applied voltage across different temperature ranges is shown in Fig. 13(a). The characteristics of the *I–V* curve are clearly non-linear which indicate a non-ohmic behavior, thereby affirming the semiconducting properties of the compound.[80] Fig. 13(b) displays leakage current density (J) with the applied electric field (E). All log J *vs.* log E curves displayed in figure are asymmetric for the positive and negative applied field caused by the varied contact conditions at the site *i.e.*, at the interfaces between the BCFZO layer and the electrodes situated at the top and bottom. This phenomenon can be elucidated by the oxygen vacancy that can shift when influenced by an external force. The leakage current of the prepared sample evaluated in both positive and negative voltage conditions is directly linked to the amount of oxygen vacancies present in the interface.[42] The increase in leakage current is due to the significant potential barrier of the function. The charge carriers within the material can disperse effortlessly at low temperatures due to the absence of any potential barrier.[72] As temperatures rise, the hopping operation of the barrier is activated, leading to eventual leakage. The correlation of temperature with the potential barrier shows that the temperature alteration could affect electron mobility and conductivity, hence influencing the leakage process significantly.[73]

The curves representing the logarithmic relationship between log(J) and log(E) in Fig. 13(c-1) illustrate various mechanisms through which leakage occurs. There exist two types of conduction mechanisms *i.e.*, ohmic conduction and space charge limited current (SCLC) conduction that mediate the log J–log E relation in a linear pattern with slope values (α) 1 and 2 respectively.

When electrons move through a barrier while being subjected to a strong electric field, this phenomenon is known as Fowler–Nordheim (FN) tunnelling. Due to the absence of thermal energy required for the charge carriers to cross the barrier, tunnelling takes over as the primary transport mode at

Table 4 Magnetic parameters of different models associated with prepared sample

		Parameters				
Model name	Expression of the model	M_s	a	b	c	χ
Akulov	$M = M_S\left(1 - \frac{b}{H^2}\right)$	3.53×10^{-4}	—	11 195.18	—	—
Brown	$M = M_S\left(1 - \frac{a}{H} - \frac{b}{H^2}\right) + \chi H$	3.87×10^{-4}	262.36	−17538.67	—	5.78×10^{-9}
Grosinger	$M = M_s\left(1 - \frac{a}{H} - \frac{b}{H^2} - \frac{c}{H^3}\right)$	4.37×10^{-4}	405.488	−69727.36	3.82×10^{6}	1.855×10^{-9}
Neel	$M = M_S\left(1 - \frac{a}{H} - \frac{b}{H^2}\right)$	4.38×10^{-4}	292.425	−20576.36	—	—

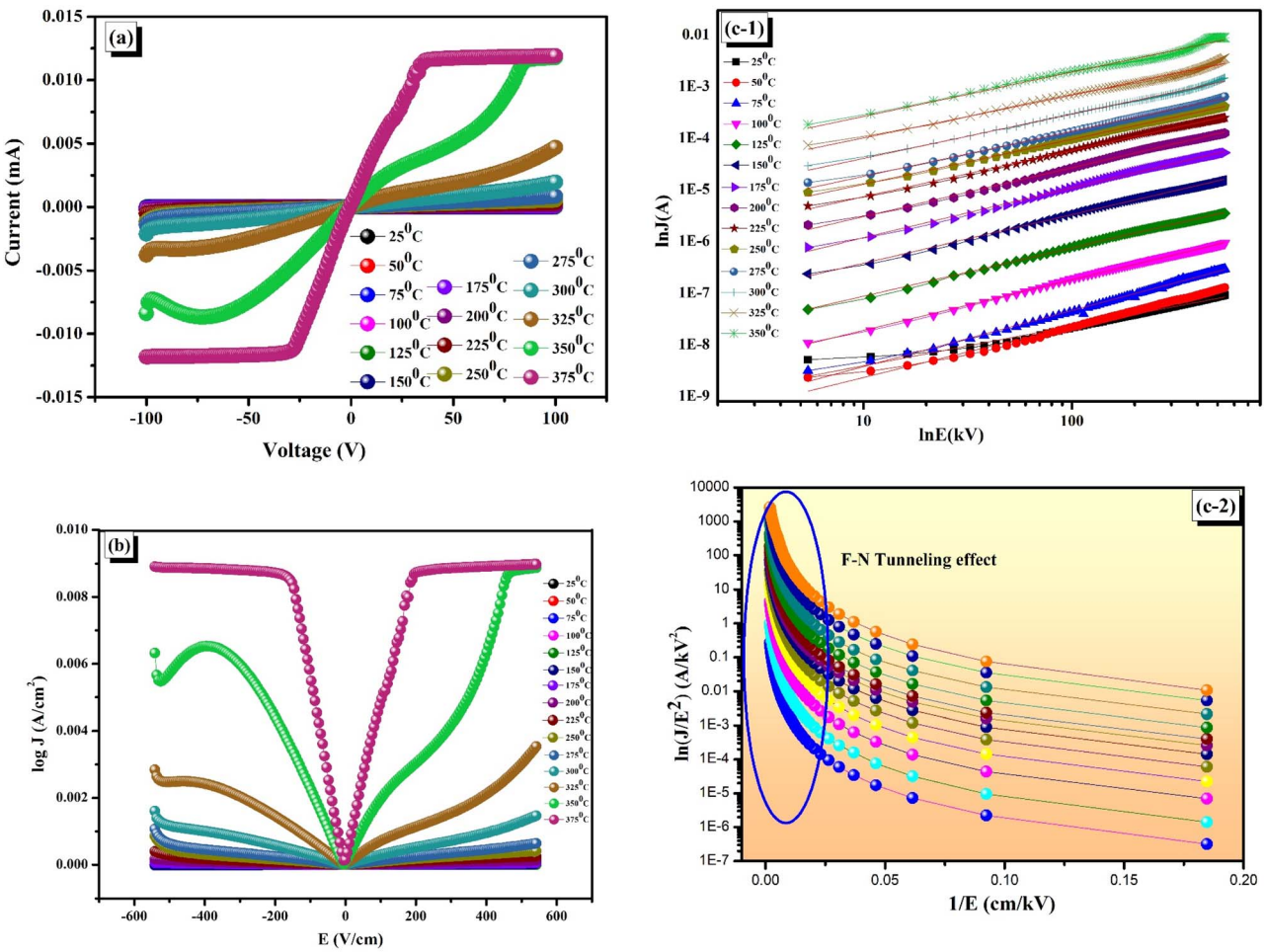

Fig. 13 (a) I–V-characteristic plot at various temperature. (b) Log J *vs.* E plot at various temperature. (c-1) Log J *vs.* log E plot at various temperature. (c-2) Log J/E^2 *vs.* E plot at various temperature.

low-temperature ranges. Tunnelling occurs directly for low bias, but when the bias is more than the barrier height, the barrier becomes triangular, which raises the tunnelling probability and causes the emission of the F–N tunnelling field. Whereas field emission results in a linear relationship with a negative slope, direct tunnelling produces a logarithmic dependence in the FN plot. From Fig. 13(c-2) the FN-tunnelling effect is prominent when the graphical representation of log J/E^2) *vs.* $1/E$ is taken into consideration, providing a direction to the increased leakage current density of the fractionally substituted double perovskite oxide.[42]

12. Conclusion

The structural and micro-structural analysis of the studied compound confirms the formation of a single-phase, high-

density sample The fabrication and characterisation of the polycrystalline ceramic sample conclude the development of a *Pcmn* space group with an orthorhombic phase. Room temperature dielectric measurements suggest that the material may be suitable for use in multilayer capacitors. The optical band gap of 2.61 eV indicates its potential applicability in photocatalytic devices. The thermistor parameters demonstrate that the compound could be used in NTC thermistor devices. Magnetic studies suggest the material may also be suitable for magnetic storage applications. Overall, the findings indicate that the compound holds promise for multifunctional applications.

Data availability

Some of the data generated during this study are included in this article. The rest datasets generated during the current study are available from the corresponding author on reasonable request.

Conflicts of interest

The authors declare that they have no known competing financial interests or personal relationships that could have appeared to influence the work reported in this paper. We declare that the manuscript is new and has not been submitted anywhere for publication. In addition to the above, we have no conflicts of interest with anybody.

References

1 E. Solana-Madruga, P. S. Kearins, C. Ritter, Á. M. Arévalo-López and J. P. Attfield, 1: 1 Ca^{2+}: Cu^{2+} A-site order in a ferrimagnetic double double perovskite, *Angew. Chem.*, 2022, **134**, e202209497.
2 M. Shaikh, A. Fathima, M. J. Swamynadhan, H. Das and S. Ghosh, Investigation into cation-ordered magnetic polar double perovskite oxides, *Chem. Mater.*, 2021, **33**, 1594–1606.
3 G. King and S. Garcia-Martin, Expanding the doubly cation ordered AA' $BB'O_6$ perovskite family: structural complexity in NaLaInNbO6 and NaLaInTaO6, *Inorg. Chem.*, 2019, **58**, 14058–14067.
4 A. Dias, G. Subodh, M. T. Sebastian, M. M. Lage and R. L. Moreira, Vibrational studies and microwave dielectric properties of A-site-substituted tellurium-based double perovskites, *Chem. Mater.*, 2008, **20**, 4347–4355.
5 G. King, S. Thimmaiah, A. Dwivedi and P. M. Woodward, Synthesis and characterization of new $AA'BWO_6$ perovskites exhibiting simultaneous ordering of A-site and B-site cations, *Chem. Mater.*, 2007, **19**, 6451–6458.
6 L. Zhang, Q. Liu, N. Ding, H. Yang, L. Wang and Q. Zhang, Dual-channel enhanced luminescence of double perovskite $NaGdMgWO_6$: Eu^{3+} phosphor based on alternative excitation and delayed quenching, *J. Alloys Compd.*, 2015, **642**, 45–52.
7 A. A. Elbadawi, O. A. Yassin, A. Gismeseed, *Cation disorder effect on the crystal structure and the Iron spin state of* $ALaFeTiO_6$ *(A = Ca, Sr and Ba) double perovskite oxide*, 2012.
8 M. C. Knapp and P. M. Woodward, A-site cation ordering in $AA'BB'O_6$ perovskites, *J. Solid State Chem.*, 2006, **179**, 1076–1085.
9 M. Amin, H. M. Rafique, M. Yousaf, S. M. Ramay and S. Atiq, Structural and impedance spectroscopic analysis of Sr/Mn modified $BiFeO_3$ multiferroics, *J. Mater. Sci.: Mater. Electron.*, 2016, **27**, 11003–11011.
10 J. Xie, C. Feng, X. Pan and Y. Liu, Structure analysis and multiferroic properties of Zr4+ doped $BiFeO_3$ ceramics, *Ceram. Int.*, 2014, **40**, 703–706.
11 S. Mukherjee, R. Gupta, A. Garg, V. Bansal and S. Bhargava, Influence of Zr doping on the structure and ferroelectric properties of $BiFeO_3$ thin films, *J. Appl. Phys.*, 2010, **107**(12), 123535.
12 P. Chandra Sati, M. Arora, S. Chauhan, S. Chhoker and M. Kumar, Structural, magnetic, and optical properties of Pr and Zr codoped $BiFeO_3$ multiferroic ceramics, *J. Appl. Phys.*, 2012, **112**(9), 094102.
13 S. Mukherjee, A. Srivastava, R. Gupta and A. Garg, Suppression of grain boundary relaxation in Zr-doped $BiFeO_3$ thin films, *J. Appl. Phys.*, 2014, **115**, DOI: **10.1063/1.4879247**.
14 S. M. A. Kader, D. E. J. Ruth, M. V. G. Babu, M. Muneeswaran, N. V Giridharan and B. Sundarakannan, Investigations on the effect of Ba and Zr co-doping on the structural, thermal, electrical and magnetic properties of $BiFeO_3$ multiferroics, *Ceram. Int.*, 2017, **43**, 15544–15550.
15 A. Kathirvel, K. N. I. Krishna, R. Ganga, A. U. Maheswari and M. Sivakumar, Enhanced magnetic, dielectric and photoconductive properties of Zr doped $BiFeO_3$ nanostructures, *Phys. E*, 2022, **142**, 115306.
16 M. Boukhari, Z. Abdelkafi, N. Abdelmoula, H. Khemakhem and N. Randrianantoandro, Enhanced dielectric and optical properties in Zn^{2}+ and Zr^{4+} co-doping $BiFeO_3$ ceramic, *J. Mater. Sci.: Mater. Electron.*, 2023, **34**, 1218.
17 G. Böttger, I. Mangelschots, E. Kaldis, P. Fischer, C. Krüger and F. Fauth, The influence of Ca doping on the crystal structure and superconductivity of orthorhombic, *J. Phys.: Condens. Matter*, 1996, **8**, 8889.
18 R. Das and R. N. P. Choudhary, Studies of structural, dielectric relaxor and electrical characteristics of lead-free double Perovskite: Gd_2NiMnO_6, *Solid State Sci.*, 2019, **87**, 18.
19 T. A. Para and S. K. Sarkar, Challenges in rietveld refinement and structure visualization in ceramics, *Adv. Ceram. Mater*, 2021, 296.
20 R. A. Young and D. B. Wiles, Profile shape functions in Rietveld refinements, *Appl. Crystallogr.*, 1982, **15**, 430–438.
21 S. Mishra, S. Sahoo, N. Kumar, A. Panigrahi, B. N. Parida and R. K. Parida, Optical, electrical and magnetic properties of double perovskite Ba_2MnTiO_6 for Optoelectronics Applications, *Mater. Chem. Phys.*, 2024, 130336.
22 M. Birkholz, *Thin Film Analysis by X-Ray Scattering*, Wiley-VCH Verlag GmbH & Co. KGaA, 2006.

23 V. D. Mote, Y. Purushotham and B. N. Dole, Williamson–Hall analysis in estimation of lattice strain in nanometer-sized ZnO particles, *J. Theor. Appl. Phys.*, 2012, **6**, 1–8.
24 S. Sahoo, S. Mishra, L. Sahoo, B. N. Parida, L. Biswal and R. K. Parida, Dielectric, electric, and magnetic response of modified bismuth ferrite-based double perovskites for NTC-thermistor application, *Ceram. Int.*, 2024, **50**, 20011–20025.
25 L. Sahoo, B. N. Parida, N. C. Nayak and R. K. Parida, Revived BBFTO double perovskite with improved dielectric properties for some possible device applications, *J. Mater. Sci.: Mater. Electron.*, 2023, **34**, 1019.
26 B. Mohanty, B. N. Parida and R. K. Parida, Multiferroic and optical spectroscopic behavior of BST in BFO environment, *J. Mater. Sci.: Mater. Electron.*, 2019, **30**, 9211–9218.
27 S. A. Dar, G. Murtaza, T. Zelai, G. Nazir, H. Alkhaldi, H. Albalawi, N. A. Kattan, M. Irfan, Q. Mahmood and Z. Mahmoud, Study of structural, electronic, magnetic, and optical properties of A_2FeMnO_6 (A = Ba, La) double perovskites, experimental and DFT analysis, *Colloids Surf., A*, 2023, **664**, 131145.
28 W. Hu, T. Li, X. Liu, D. Dastan, K. Ji and P. Zhao, 1550 nm pumped upconversion chromaticity modulation in Er^{3+} doped double perovskite $LiYMgWO_6$ for anti-counterfeiting, *J. Alloys Compd.*, 2020, **818**, 152933.
29 B. N. Parida, R. K. Parida and A. B. Panda, Multi-ferroic and optical spectroscopy properties of $(Bi_{0.5}Sr_{0.5})(Fe_{0.5}Ti_{0.5})O_3$ solid solution, *J. Alloys Compd.*, 2017, **696**, 338–344.
30 L. Sahoo, B. Mohanty, B. N. Parida, N. C. Nayak and R. K. Parida, Enhanced room temperature relative permittivity and low dielectric loss ferroelectric double perovskite for energy storage applications, *Mater. Sci. Eng. B*, 2023, **294**, 116561.
31 M. A. Amin, G. Nazir, Q. Mahmood, J. Alzahrani, N. A. Kattan, A. Mera, H. Mirza, A. Mezni, M. S. Refat and A. A. Gobouri, Study of double perovskites X_2InSbO_6 (X = Sr, Ba) for renewable energy; alternative of organic-inorganic perovskites, *J. Mater. Res. Technol.*, 2022, **18**, 4403–4412.
32 A. Sasmal, S. Sen and P. S. Devi, Significantly suppressed leakage current and reduced band gap of $BiFeO_3$ through Ba–Zr Co-Substitution: Structural, optical, electrical and magnetic study, *Mater. Chem. Phys.*, 2020, **254**, 123362.
33 P. C. Sati, M. Kumar and S. Chhoker, Phase Evolution, Magnetic, Optical, and Dielectric Properties of Zr-Substituted $Bi_{0.9}Gd_{0.1}FeO_3$ Multiferroics, *J. Am. Ceram. Soc.*, 2015, **98**, 1884–1890.
34 C.-H. Yang, D. Kan, I. Takeuchi, V. Nagarajan and J. Seidel, Doping $BiFeO_3$: approaches and enhanced functionality, *Phys. Chem. Chem. Phys.*, 2012, **14**, 15953–15962.
35 Z. Ma, H. Liu, L. Wang, F. Zhang, L. Zhu and S. Fan, Phase transition and multiferroic properties of Zr-doped BiFeO 3 thin films, *J. Mater. Chem. C*, 2020, **8**, 17307–17317.
36 L. Sahoo, S. Sahoo, S. Mishra, N. C. Nayak, B. N. Parida and R. K. Parida, Structural, electrical, and multiferroic investigations of $MgBiFeTiO_6$ double perovskite for possible optoelectronic applications, *J. Mater. Sci.: Mater. Electron.*, 2024, **35**, 2167.
37 B. Mohanty, S. Sahoo, S. Mishra, S. Prasad, H. Chouhan, B. N. Parida, M. Mahapatra, R. Padhee, N. C. Nayak and R. K. Parida, Structural, electrical, and multiferroic characteristics of SFO-BST perovskite for device application, *Appl. Phys. A:Mater. Sci. Process.*, 2024, **130**, 947.
38 M. Boukhari, Z. Abdelkafi, N. Abdelmoula, H. Khemakhem and N. Randrianantoandro, Enhanced dielectric and optical properties in Zn^{2+} and Zr^{4+} co-doping $BiFeO_3$ ceramic, *J. Mater. Sci.: Mater. Electron.*, 2023, **34**, 1218.
39 S. Sen, A. Mondal, R. K. Parida and B. N. Parida, Improved optical, dielectric, impedance, and magnetic properties of $(BiFeO_3)_{0.6}(CaTiO_3)_{0.4}$ for multifunctional utilities, *Inorg. Chem. Commun.*, 2022, **142**, 109664.
40 A. K. Panda, L. Sahoo, R. Chakravarty, N. C. Nayak, R. K. Parida, B. N. Parida and R. Dutta, Transport and semiconducting behavior of Ca_2BiNbO_6 new inorganic double perovskite, *Appl. Phys. A:Mater. Sci. Process.*, 2021, **127**, 1–11.
41 S. Karmakar, B. Panda, B. Sahoo, K. L. Routray, S. Varma and D. Behera, A study on optical and dielectric properties of Ni–ZnO nanocomposite, *Mater. Sci. Semicond. Process.*, 2018, **88**, 198–206.
42 V. Dimitrov and S. Sakka, Linear and nonlinear optical properties of simple oxides. II, *J. Appl. Phys.*, 1996, **79**, 1741–1745.
43 S. Sahoo, L. Sahoo, N. C. Nayak, B. N. Parida and R. K. Parida, Investigation of the structural, dielectric, magnetic properties and NTC-thermistor response of $CaBiFeMnO_6$ double perovskites, *Mater. Adv.*, 2024, 5442–5457.
44 L. Sahoo, B. Mohanty, B. N. Parida, N. C. Nayak and R. K. Parida, Enhanced room temperature relative permittivity and low dielectric loss ferroelectric double perovskite for energy storage applications, *Mater. Sci. Eng. B*, 2023, **294**, 116561.
45 Y. Kumar, J. Pal, P. S. Malhi and R. Kumar, Enhanced electrical conductivity in Zr-Doped $(La_{0.7}Ba_{0.3})(Mn_{0.5}Fe_{0.5})O_3$ solid solutions, *J. Adv. Dielectr.*, 2020, **10**, 2050032.
46 S. Abass, A. Bagri and K. Sultan, Modifications induced in structural, electronic and dielectric properties of Nd_2NiMnO_6 double perovskite by Sr doping, *J. Alloys Compd.*, 2023, **930**, 167463.
47 S. A. U. Islam, F. A. Andrabi, F. Mohmed, K. Sultan, M. Ikram and K. Asokan, Ba doping induced modifications in the structural, morphological and dielectric properties of double perovskite La_2NiMnO_6 ceramics, *J. Solid State Chem.*, 2020, **290**, 121597.
48 K. I. Nassar, M. Slimi, N. Rammeh, A. Bouhamed, A. Njeh and O. Kanoun, Investigation of AC electrical conductivity and dielectric properties of $BiBaFeZnO_6$ double perovskite oxides, *J. Mater. Sci.: Mater. Electron.*, 2021, **32**, 24050–24057.
49 M. Z. Halizan and Z. Mohamed, Dielectric, AC conductivity, and DC conductivity behaviours of Sr_2CaTeO_6 Double Perovskite, *Materials*, 2022, **15**, 4363.

50 A. Bendahhou, K. Chourti, M. Loutou, S. El Barkany and M. Abou-Salama, Impact of rare earth (RE^{3+} = La^{3+}, Sm^{3+}) substitution in the A site perovskite on the structural, and electrical properties of Ba $(Zr_{0.9}Ti_{0.1})O_3$ ceramics, *RSC Adv.*, 2022, **12**, 10895–10910.

51 B. Mohanty, B. N. Parida and R. K. Parida, Structural and conduction behaviour of $(BaSr)_{0.5}TiO_3$ modified in BFO perovskite, *Mater. Chem. Phys.*, 2019, **225**, 91–98.

52 S. Bhattacharjee, B. Mohanty, R. K. Parida and B. N. Parida, Multifunctional feature of double perovskite strontium iron vanadate for storage device, *Mater. Chem. Phys.*, 2022, **275**, 125254.

53 S. Sen, R. K. Parida and B. N. Parida, The enhanced multifunctional behavior in G-type antiferromagnetic $BiFeO_3$ due to the modification by $MgTiO_3$, *Phys. B*, 2023, **650**, 414559.

54 S. Hcini, S. Khadhraoui, A. Triki, S. Zemni, M. Boudard and M. Oumezzine, Impedance spectroscopy properties of $Pr_{0.67}A_{0.33}MnO_3$ (A = Ba or Sr) perovskites, *J. Supercond. Novel Magn.*, 2014, **27**, 195–201.

55 A. Prasad, R. K. Mishra, K. P. Chandra and K. Prasad, Structure and electrical properties of $(Bi, Na)_{0.94}Ba_{0.06}Ti_{1-x}(Mg_{1/3}Nb_{2/3})xO_3$ ceramics, *Process. Appl. Ceram.*, 2018, **12**, 383–393.

56 S. G. Infantiya, A. Aslinjensipriya, R. S. Reena, K. J. Pious, P. Sivakumar, C. J. Raj and S. J. Das, Probing the structural and electrical traits of lead-free Zn/Mn co-substituted $CaCu_3Ti_4O_{12}$-based perovskite ceramics, *J. Mater. Sci.: Mater. Electron.*, 2023, **34**, 1994.

57 R. Chakravarty, H. Talukdar, P. Phukan, R. K. Parida and B. N. Parida, Effect of 'Ca' in dielectric, optical, and magnetic behavior of $BaFe_{0.5}Nb_{0.5}O_3$ for possible device applications, *Vacuum*, 2023, **216**, 112415.

58 E. K. Abdel-Khalek, E. A. Mohamed, S. M. Salem and I. Kashif, Structural and dielectric properties of $(100 - x)$ B_2O_3-$(x/2)Bi_2O3$–$(x/2)Fe_2O_3$ glasses and glass-ceramic containing BiFeO3 phase, *J. Non-Cryst. Solids*, 2018, **492**, 41–49.

59 M. Priyadarsini, M. Mahapatra, R. K. Parida and R. Padhee, Dielectric, structural and optical properties of lead-free $Ba_4(Dy_{2-x}Bi_x)Fe_2Nb_8O_{30}$ ferroelectrics, *Phase Transitions*, 2024, 1–22.

60 H. Chouhan, S. Prasad, S. Parthasarathy, R. Chakravarty, M. M. Borgohain, S. Bhattacharjee, R. K. Parida, S. Behera and B. N. Parida, Unveiling the potential of a novel inorganic perovskite for NTC thermistor and energy-storage applications, *Inorg. Chem. Commun.*, 2024, **170**, 113127.

61 J. Wang, H. Zhang, D. Xue and Z. Li, Electrical properties of hexagonal $BaTi_{0.8}Co_{0.2}O_{3-\delta}$ ceramic with NTC effect, *J. Phys. D Appl. Phys.*, 2009, **42**, 235103.

62 S. Mishra, R. N. P. Choudhary and S. K. Parida, Structural, dielectric, electrical and optical properties of Li/Fe modified barium tungstate double perovskite for electronic devices, *Ceram. Int.*, 2022, **48**, 17020–17033.

63 S. S. Hota, D. Panda and R. N. P. Choudhary, Structural, topological, dielectric, and electrical properties of a novel calcium bismuth tungstate ceramic for some device applications, *J. Mater. Sci.: Mater. Electron.*, 2023, **34**, 900.

64 S. Sahoo, L. Sahoo, T. R. Rautray, B. N. Parida and R. K. Parida, Structural, dielectric characterization of $BaFe_2MnO_6$ double perovskite, *Ferroelectrics*, 2024, **618**(1), 38–46.

65 L. Sahoo, S. Sahoo, R. Chakravarty, N. Saikia, B. N. Parida and R. K. Parida, Multiferroic and Electrical Properties of Mg^{2+} Substituted Lead-Free Double Perovskite for Device-Based Utilizations, *J. Inorg. Organomet. Polym. Mater.*, 2024, **34**, 2260–2275.

66 B. Mohanty, B. N. Parida and R. K. Parida, Structural, dielectric and magnetic behavior of BST modified rare earth ortho-ferrite $LaFeO_3$, *Ceram. Int.*, 2020, **46**, 16502–16509.

67 B. Mohanty, B. N. Parida and R. K. Parida, Multiferroic and optical spectroscopic behavior of BST in BFO environment, *J. Mater. Sci.: Mater. Electron.*, 2019, **30**, 9211–9218.

68 L. Sahoo, S. Sahoo, S. Mishra, N. C. Nayak, B. N. Parida and R. K. Parida, Structural, electrical, and multiferroic investigations of $MgBiFeTiO_6$ double perovskite for possible optoelectronic applications, *J. Mater. Sci.: Mater. Electron.*, 2024, **35**, DOI: **10.1007/s10854-024-13867-9**.

69 B. Mohanty, S. Bhattacharjee, S. N. Sarangi, N. C. Nayak, R. K. Parida and B. N. Parida, Dielectric, electrical and magnetic characteristics of BST modified BLFO lead free ceramic, *J. Alloys Compd.*, 2021, **863**, 158060.

70 M. Shakir, B. K. Singh, R. K. Gaur, B. Kumar, G. Bhagavannarayana and M. A. Wahab, Dielectric behaviour and ac electrical conductivity analysis of ZnSe chalcogenide nanoparticles, *Chalcogenide Lett.*, 2009, **6**, 655–660.

71 S. Sahoo, S. K. S. Parashar and S. M. Ali, $CaTiO_3$ nano ceramic for NTCR thermistor based sensor application, *J. Adv. Ceram.*, 2014, **3**, 117–124.

72 S. S. Hota, D. Panda and R. N. P. Choudhary, Study of synthesis and characterization of triple ions modified bismuth ferrite for electronic devices:$(Bi_{1/2}Li_{1/2})(Fe_{1/3}Mn_{1/3}W_{1/3})$ O_3, *Solid State Ionics*, 2023, **399**, 116313.

73 S. M. A. Kader, D. E. J. Ruth, M. V. G. Babu, M. Muneeswaran, N. V Giridharan and B. Sundarakannan, Investigations on the effect of Ba and Zr co-doping on the structural, thermal, electrical and magnetic properties of BiFeO3 multiferroics, *Ceram. Int.*, 2017, **43**, 15544–15550.

74 M. Kumar, M. Arora, S. Chauhan and S. Joshi, Raman spectroscopy probed spin-two phonon coupling and improved magnetic and optical properties in Dy and Zr substituted $BiFeO_3$ nanoparticles, *J. Alloys Compd.*, 2017, **692**, 236–242.

75 M. K. Sharif, M. A. Khan, A. Hussain, F. Iqbal, I. Shakir, G. Murtaza, M. N. Akhtar, M. Ahmad and M. F. Warsi, Synthesis and characterization of Zr and Mg doped $BiFeO_3$ nanocrystalline multiferroics *via* micro emulsion route, *J. Alloys Compd.*, 2016, **667**, 329–340.

76 A. B. CAHAYA and A. Manaf, Law of Approach to Saturation for Determining Magnetic Intrinsic Behavior of BaFe12–xMnx/2Tix/2O_{19} and SrFe12–xMnx/2Tix/2O_{19}, Al-Fiziya:

journal of Materials Science, *Geophys. Instrum.Theor. Phys.*, 2022, **4**, 78–82.

77 S. Bhattacharyya, S. S. N. Bharadwaja and S. B. Krupanidhi, Alternating current conduction behavior of excimer laser ablated $SrBi_2Nb_2O_9$ thin films, *J. Appl. Phys.*, 2000, **88**(7), 4294–4302.

78 D. C. Sinclair and A. R. West, Impedance and modulus spectroscopy of semiconducting $BaTiO_3$ showing positive temperature coefficient of resistance, *J. Appl. Phys*, 1989, **66**, 3850–3856.

79 R. Metz, Electrical properties of N. T. C. thermistors made of manganite ceramics of general spinel structure: $Mn_{3-x-x'}M_xN_{x'}O4$ ($0 \leq x + x' \leq 1$; M and N being Ni, Co or Cu). Aging phenomenon study, *J. Mater Sci.*, 2000, **35**, 4705–4711.

80 S. Subhanarayan, Negative temperature coefficient resistance of $CaTiO_3$ for thermistor application, *Trans. Electr. Electron. Mater*, 2020, **21**, 91–98.

81 Z. Z. Ma, Z. M. Tian, J. Q. Li, C. H. Wang, S. X. Huo, H. N. Duan and S. L. Yuan, Enhanced polarization and magnetization in multiferroic $(1 - x)BiFeO_3$–$xSrTiO_3$ solid solution, *Solid Stat. Sci.*, 2011, **13**, 2196–2200, DOI: 10.1016/j.solidstatesciences.2011.10.008.

82 S. V. Streltsov and D. I. Khomskii, *Electronic structure and magnetic properties of pyroxenes (Li, Na) TM (Si, Ge) $2O_6$: novel low-dimensional magnets with 90 bonds*, arXiv preprint arXiv:0710.5351, 2007.

83 C. Yang, C. Z. Liu, C. M. Wang, W. G. Zhang and J. S. Jiang, Magnetic and dielectric properties of alkaline earth Ca_{2+} and Ba_{2+} ions co-doped $BiFeO_3$ nanoparticles, *Journal of magnetism and magnetic materials*, 2012, **324**(8), 1483–1487.

84 A. K. Singh, S. Chauhan, S. K. Srivastava and R. Chandra, Influence of antisite disorders on the magnetic properties of double perovskite Nd_2NiMnO_6, *Solid State Commun.*, 2016, **242**, 74–78.

85 H. Ouyang, Y.-H. Han, S.-C. Lo, C.-H. Su, Y.-R. Shiu, K.-W. Lin, R. D. Desautels and J. Van Lierop, ailoring perpendicular magnetic anisotropy in ultrathin Co/Pt multilayers coupled to NiO, *Phys. Rev. B: Condens. Matter Mater. Phys.*, 2010, **81**(22), 224412.